Bifurcation analysis of steady Rayleigh–Bénard convection in a cubical cavity with conducting sidewalls

DOLORS PUIGJANER[1], JOAN HERRERO[2], CARLES SIMÓ[3] AND FRANCESC GIRALT[2]

[1]Dept. Eng. Informàtica i Matemàtiques, Univ. Rovira i Virgili, Tarragona, Catalunya, Spain
[2]Dept. Enginyeria Quimica, Univ. Rovira i Virgili, Tarragona, Catalunya, Spain
[3]Dept. Matemàtica Aplicada i Anàlisi, Univ. de Barcelona, Barcelona, Catalunya, Spain

Natural convection in a cubical cavity heated from below with perfectly conducting sidewalls is investigated numerically. A parameter continuation procedure based on a Galerkin spectral method was applied to obtain the bifurcation diagrams for steady flow solutions over the region of Rayleigh numbers $Ra \leqslant 1.5 \times 10^5$ at Prandtl numbers $Pr = 0.71$ and 130. In both cases, the bifurcation diagrams were more complex than those previously reported for adiabatic sidewalls. Four and nine different convective solutions (without taking into account the solutions obtained by symmetry) that were stable over certain ranges of Ra were respectively identified at $Pr = 0.71$ and 130. The dependence of the bifurcation diagrams and of the topology of the flow patterns on the Prandtl number were also stronger in the case of conducting sidewalls. Most of the flow patterns investigated evolved to double toroid-like topologies with increasing Rayleigh number. This is especially noticeable at $Pr = 130$, where all flow patterns adopted double-toroid shapes that were superimposed on the characteristic flow patterns observed at values of Ra slightly above the respective bifurcation points where they originated. At sufficiently high Ra the double-toroid pattern configuration prevailed. This phenomenon, which has not been previously observed in the case of adiabatic lateral walls, is related to the thermal activity of the sidewalls, which locally extract/supply relatively large amounts of heat from/to the fluid. These predictions are consistent with experimental flow transitions and topologies reported in the literature. In addition, a complete bifurcation study in the two-dimensional (Ra, Pr)-plane was carried out for the flow pattern with an initial configuration of four connected half-rolls which was stable at both $Pr = 0.71$ and 130. Since the surface of Nu over the (Ra, Pr)-plane presented several folds and cusps, different regions were identified as a function of the number of particular realizations of this flow pattern, varying between zero and five. Three different regions of stability were identified for this particular flow pattern in the (Ra, Pr)-plane within the range of parameters investigated, i.e. $Ra \leqslant 1.5 \times 10^5$ and $0.71 \leqslant Pr \leqslant 130$.

1. Introduction

Rayleigh–Bénard convection in confined enclosures has been extensively studied (Yang 1988; Koschmieder 1993; Getling 1998; Bodenschatz, Pesch & Ahlers 2000) because of its practical applications and theoretical relevance. Since natural convection constitutes a fluid flow problem with well-established base solutions

for the velocity and temperature fields, for certain simple geometries and thermal boundary conditions, it provides an appropriate model for the study of hydrodynamic instabilities and subsequent flow bifurcations preceding the onset of turbulence. The first bifurcation, corresponding to the instability of the motionless conductive state and the onset of convection, occurs when the Rayleigh number reaches a critical value Ra_c. In the case of confined domains the critical Rayleigh number depends not only on the geometry but also on the thermal boundary conditions. Several numerical linear stability analyses carried out previously have determined the variation of Ra_c with the width/height and length/height aspect ratios for parallelepipedical cavities with either perfectly conducting (Davis 1967; Catton 1972; Mizushima & Nakamura 2003) or adiabatic lateral walls (Catton 1970; Gelfgat 1999). These studies also identified the flow patterns developed at Ra slightly above the critical value. Nevertheless, reliable information about the flow transitions that occur as the Rayleigh number is further increased is still missing in most cases since numerical parameter continuation and bifurcation methods applied to the nonlinear governing equations have not been carried out.

Flows in cubical cavities are particularly interesting because the intrinsic symmetry of this geometry yields steady-state solutions with more symmetries than those found in parallelepipedical enclosures (Leong, Hollands & Brunger 1999; Pallarès *et al.* 2001; Pepper & Hollands 2002; Mizushima & Nakamura 2003). Also, given a solution in a cubical cavity, several other solutions can be obtained by considering the geometrical symmetries. The bifurcation analyses reported by Puigjaner *et al.* (2004, 2006) reveal that the bifurcation diagrams of steady flow patterns that develop inside a cubical cavity with adiabatic lateral walls and filled either with air ($Pr = 0.71$) or silicone oil ($Pr = 130$) are rather complex. Five and six flow patterns (enumerating only those that are not related by symmetries of the problem) were respectively identified to be stable over some ranges of the Rayleigh number within the region $Ra \leqslant 1.5 \times 10^5$ at $Pr = 0.71$ and 130. Several steady flow patterns and several flow transitions were experimentally observed by Pallarès *et al.* (2001) in a cubical cavity filled with silicone oil ($Pr = 130$) with both adiabatic and perfectly conducting lateral walls. Most of the experimental flow transitions between different steady flow patterns observed by these authors for $Ra \leqslant 8 \times 10^4$ and adiabatic lateral walls were explained by the bifurcation diagram reported in Puigjaner *et al.* (2006).

The difficulty in building an experimental set-up with either perfectly adiabatic or perfectly conducting lateral walls may explain some of the discrepancies between computed and measured results for convection in cavities (Leong, Hollands & Brunger 1998). One consequence of the lateral walls being conductive is that part of the heat transferred from the bottom to the top wall flows through the lateral walls. The effect of sidewall conductance on the heat transport characteristics of confined turbulent flows was theoretically investigated by Ahlers (2000) and Roche *et al.* (2001). Both proposed definitions of the Nusselt number that take into account the rate of total heat transfer through the lateral walls. On the other hand, the effects of a sidewall with finite thermal conductivity on flows confined in a cylindrical cavity were numerically studied by Verzicco (2002). This author expressed the thermal boundary conditions as a function of the heat conductivity of the sidewall, which varied from adiabatic to highly conducting. Verzicco (2002) showed that the heat conductivity of the sidewall not only affected the Nusselt number but also the topology of the mean flow structures.

The aim of the present study is to determine the bifurcation diagrams of steady convective flow patterns in a cubical cavity with perfectly conducting lateral walls at

both $Pr = 0.71$ and 130 for $Ra \leqslant 1.5 \times 10^5$. The stability and domains of existence of the steady solutions that arise at bifurcation points are calculated. Stable and unstable steady solution branches are tracked using an arclength continuation algorithm applied to the nonlinear steady governing equations obtained by means of a Galerkin method. Both steady and Hopf bifurcation points are determined along the different bifurcating branches. Initially unstable steady flow patterns are also tracked since they can become stable as a consequence of subsequent bifurcations (see Puigjaner *et al.* 2004, 2006). The study of the evolution of the spatial configuration of flow patterns as Ra is increased focuses on those flow patterns that are stable over certain ranges within the studied domain. Since the evolutions of flow patterns may be quite different from those reported by Puigjaner *et al.* (2004, 2006) for adiabatic lateral walls, the effect of thermal boundary conditions on the flow and heat transport characteristics is analysed for different flow patterns. On the other hand, Puigjaner *et al.* (2006) showed that the dependence of the flow patterns and heat transport characteristics on the Prandtl number was significant but smooth when adiabatic lateral walls were assumed. To illustrate the complex dependence of the current bifurcation diagrams on Pr a comprehensive bifurcation study in the two-dimensional (Ra, Pr) parameter plane is presented for the stable flow pattern of four connected half-rolls. Moreover, predicted flow patterns and transitions are compared with the experimental results reported by Leong *et al.* (1999) at $Pr = 0.71$ and Pallarès *et al.* (2001) at $Pr = 130$.

2. Governing equations and numerical method

2.1. *Governing equations*

The problem of an incompressible flow of a Newtonian fluid confined in a cubical cavity with six rigid walls is investigated. The top and the bottom horizontal walls are kept at the constant temperatures T_c and T_h ($T_c < T_h$), respectively, and the lateral walls are assumed to be perfectly conducting, i.e. a linear vertical temperature profile is assumed. The non-dimensional domain scaled by the length of the cubical cavity, L, is represented by $D = [-1/2, 1/2] \times [-1/2, 1/2] \times [-1/2, 1/2]$.

The problem is governed by mass conservation, Navier–Stokes and energy conservation equations. The non-dimensional equations depend on two dimensionless parameters, the Rayleigh number, Ra, and the Prandtl number, Pr, which control the physics and, hence, the solutions of the problem. These parameters are defined as $Ra = \beta(\Delta T)gL^3/\alpha\nu$ and $Pr = \nu/\alpha$, where g is the acceleration due to gravity, β is the coefficient of thermal expansion, ν is the kinematic viscosity, α is the thermal diffusivity and $\Delta T = T_h - T_c$. Assuming the Boussinesq approximation, i.e. all fluid properties are constant except for a linear variation of density (ρ) with temperature in the buoyancy term of the Navier–Stokes equations, the governing dimensionless nonlinear equations for the velocity $V = (u, v, w)$, the temperature departure from the motionless conductive state, $\theta = [T - (T_h + T_c)/2]/\Delta T - z$, and pressure, p, are

$$Pr^{-1}\left(\frac{\partial V}{\partial t} + Ra^{1/2}(V \cdot \nabla)V\right) - \nabla^2 V - Ra^{1/2}\theta \, e_z + \nabla p = 0, \quad (2.1a)$$

$$\frac{\partial \theta}{\partial t} + Ra^{1/2}(V \cdot \nabla)\theta - \nabla^2\theta - Ra^{1/2}w = 0, \quad (2.1b)$$

$$\nabla \cdot V = 0, \quad (2.1c)$$

subject to boundary conditions

$$u = v = w = \theta = 0 \quad \text{along} \quad |x| = 1/2, \ |y| = 1/2, \ |z| = 1/2. \quad (2.1d)$$

The dimensionless equations (2.1a–d) are obtained by taking $q_0 = [\beta(\Delta\theta)gL\alpha/\nu]^{1/2}$, $\Delta\theta$, L^2/α and $\rho\nu q_0/L$ as characteristic scales for velocity, temperature, time and pressure, respectively. In (2.1a) $\boldsymbol{e}_z$ denotes the unit vector in the z-direction.

2.2. *Symmetry properties*

The current study covers both symmetric and non-symmetric solutions. Nevertheless, the underlying symmetries of the problem, described in this section, have been used to reduce the computational effort and to understand the spatial configuration of flow patterns that arise at subsequent bifurcations as Ra is increased. The consistency of the symmetry properties of those flow patterns that set in at symmetry-breaking bifurcations has also been checked.

The domain D and equations (2.1a–d) are respectively invariant and equivariant under the reflections $\boldsymbol{S}_x$, $\boldsymbol{S}_y$, $\boldsymbol{S}_z$ and $\boldsymbol{S}_{d_+}$ about the planes $x = 0$, $y = 0$, $z = 0$ and $x = y$, respectively. The actions of these symmetries on solutions of (2.1a–d) are

$$\left.\begin{array}{ll} \boldsymbol{S}_x : (x, y, z) \quad \rightarrow (-x, y, z) & \boldsymbol{S}_y : (x, y, z) \quad \rightarrow (x, -y, z) \\ \quad\;\; (u, v, w, \theta) \rightarrow (-u, v, w, \theta), & \quad\;\; (u, v, w, \theta) \rightarrow (u, -v, w, \theta) \end{array}\right\} \quad (2.2a,b)$$

$$\left.\begin{array}{ll} \boldsymbol{S}_z : (x, y, z) \quad \rightarrow (x, y, -z) & \boldsymbol{S}_{d_+} : (x, y, z) \quad \rightarrow (y, x, z) \\ \quad\;\; (u, v, w, \theta) \rightarrow (u, v, -w, -\theta), & \quad\;\;\; (u, v, w, \theta) \rightarrow (v, u, w, \theta) \end{array}\right\} \quad (2.2c,d)$$

The above elements generate the symmetry group $D_{4h} = Z_2 \times D_4$, where Z_2 is generated by the reflection about the horizontal midplane, $\boldsymbol{S}_z$, and D_4 is the dihedral group, which is the symmetry group of a square. Since the two reflections $\boldsymbol{S}_y$ and $\boldsymbol{S}_{d_+}$ do not commute they are sufficient to generate D_4. Note that the same symbol is used to denote equivalent symmetries in $\mathbb{R}$, $\mathbb{R}^2$ and $\mathbb{R}^3$. In $\mathbb{R}^3$, $\boldsymbol{S}_{d_+} \cdot \boldsymbol{S}_y = \boldsymbol{R}$ while $\boldsymbol{S}_y \cdot \boldsymbol{S}_{d_+} = \boldsymbol{R}^{-1}$, where $\boldsymbol{R}$ is a rotation of angle $\pi/2$ around the z-axis. The symmetry with respect to the origin and a rotation of angle π around the y-axis are respectively denoted as $-\boldsymbol{I} = \boldsymbol{R}^2 \cdot \boldsymbol{S}_z$ and $-\boldsymbol{S}_y = -\boldsymbol{I} \cdot \boldsymbol{S}_y$. Thus, the group D_{4h} contains sixteen elements: the four rotations $\boldsymbol{R}^k$, $k = 0, 1, 2, 3$; the five reflections $\boldsymbol{S}_{d_+}$, $\boldsymbol{S}_{d_-}$, $\boldsymbol{S}_x$, $\boldsymbol{S}_y$ and $\boldsymbol{S}_z$; and the products of these nine elements with the central symmetry $-\boldsymbol{I}$ (note that $\boldsymbol{R}^4 = \boldsymbol{I}$ and $-\boldsymbol{I} \cdot \boldsymbol{R}^2 = \boldsymbol{S}_z$).

The expression $\boldsymbol{S}B = (\boldsymbol{S}V, \boldsymbol{S}(\theta e_z) \cdot \boldsymbol{e}_z)$ is a steady solution of (2.1a–d) if $B = (V, \theta)$ is also a steady solution and $\boldsymbol{S} \in D_{4h}$ is a symmetry of the problem. This solution satisfies either $\boldsymbol{S}B \neq B$, in which case a different steady solution is generated, or $\boldsymbol{S}B = B$, in which case $\boldsymbol{S}$ is a symmetry of the solution B. Consequently, up to fifteen additional solutions can be generated from a particular solution of (2.1a–d) by using the symmetry properties of the problem. The set of all solution $\boldsymbol{S}B$ for $\boldsymbol{S} \in D_{4h}$ is called the orbit of the solution B under D_{4h}. On the other hand, the symmetries of any particular solution B form a subgroup of D_{4h} called the isotropy subgroup of the solution which is denoted Σ_B. The number of distinct solutions in the orbit of a solution B is $16/|\Sigma_B|$, where $|\Sigma_B|$ indicates the order of Σ_B. Solutions on the same orbit have conjugate isotropy subgroups, i.e. $\Sigma_{\boldsymbol{S}B} = \boldsymbol{S}\Sigma_B\boldsymbol{S}^{-1}$. Only one particular solution of those in the same orbit has been considered in the current study. The remaining solutions and their symmetries can be determined by applying the symmetries of the problem and the conjugacy relationship.

In the current study the ensemble of all solutions in the same orbit is referred to as a *flow pattern*. Once a flow pattern sets in the name or identifier is kept along the continuation branch with respect to Ra or Pr. A flow pattern is the set of all spatial configurations obtained by continuation with respect to Ra and Pr and should not

be understood as a particular spatial configuration for a unique value of these two parameters.

2.3. *Numerical method*

The continuation procedure reported by Puigjaner *et al.* (2004) was applied to determine the bifurcations and stability of the steady solutions ($\partial \boldsymbol{V}/\partial t = 0$, $\partial \theta/\partial t = 0$) of equations (2.1 *a–d*). This procedure, which is briefly described in this section, was based on a Galerkin spectral method with a complete, divergence-free set of basis functions satisfying all boundary conditions. A formulation of the velocity field in terms of three scalar potential functions (see Kessler 1987; Puigjaner *et al.* 2004) was used to obtain an appropriate set of divergence-free basis functions to expand the velocity vector field $\boldsymbol{V}$.

The velocity and temperature fields were approximated by the truncated expansion

$$\begin{pmatrix} \boldsymbol{V} \\ \theta \end{pmatrix} = \sum_{i=1}^{N_x} \sum_{j=1}^{N_y} \sum_{k=1}^{N_z} \sum_{s=1}^{4} a_{ijk}^{(s)} \boldsymbol{G}_{ijk}^{(s)}, \tag{2.3}$$

where $a_{ijk}^{(s)}$ are the unknown time-dependent coefficients, and $\boldsymbol{G}_{ijk}^{(s)}$ are defined as

$$\boldsymbol{G}_{ijk}^{(1)} = \begin{pmatrix} 0 \\ -g_i(x)f_j(y)f_k'(z) \\ g_i(x)f_j'(y)f_k(z) \\ 0 \end{pmatrix}, \quad \boldsymbol{G}_{ijk}^{(2)} = \begin{pmatrix} -f_i(x)g_j(y)f_k'(z) \\ 0 \\ f_i'(x)g_j(y)f_k(z) \\ 0 \end{pmatrix}, \tag{2.4a,b}$$

$$\boldsymbol{G}_{ijk}^{(3)} = \begin{pmatrix} -f_i(x)f_j'(y)h_k'(z) \\ f_i'(x)f_j(y)h_k'(z) \\ 0 \\ 0 \end{pmatrix}, \quad \boldsymbol{G}_{ijk}^{(4)} = \begin{pmatrix} 0 \\ 0 \\ 0 \\ g_i(x)g_j(y)g_k(z) \end{pmatrix}. \tag{2.4c,d}$$

The functions with superscript $s = 1, 2, 3$ refer to velocity components, while $s = 4$ concerns the temperature. In (2.4 *a–d*) the functions f are the so-called beam functions documented by Harris & Reid (1958), and the functions g and h are the trigonometric functions

$$\left. \begin{array}{ll} g_k(x): & \cos((2k-1)\pi x) \quad \text{or} \quad \sin(2k\pi x), \\ h_k(x): & \cos(2(k-1)\pi x) \quad \text{or} \quad \sin((2k-1)\pi x). \end{array} \right\} \tag{2.5}$$

The values of N_x, N_y, N_z used in the current calculations are, typically, of the form $2m$ (it is useful to consider the parity of the functions) with $m = 7$. This gives a total set of $4 \times 14^3 = 11\,076$ basis functions.

The thermal boundary conditions assumed in the current study are different from those used in Puigjaner *et al.* (2004) and the basis functions involved in the expansion of the temperature field have been modified to fulfil the thermal boundary conditions defined in (2.1 *d*). The temperature field was approximated by the expansion

$$\theta = \sum_{i,j,k} a_{ijk}^{(4)} g_i(x)g_j(y)g_k(z). \tag{2.6}$$

The Galerkin method transforms the partial differential equations (2.1*a–d*) into a system of ordinary differential equations whose unknowns are the time-dependent coefficients used to expand the velocity and temperature fields. For steady solutions the problem reduces to the nonlinear vector equation,

$$\boldsymbol{f}(\boldsymbol{c}, Ra, Pr) = 0, \tag{2.7a}$$

$Ra/10^3$	Nu	$\Delta(\%)$	$Ra/10^3$	Nu	$\Delta(\%)$	Flow pattern
44	2.047	0.4	150	2.423	1.4	B_1
91	3.999	2.8	150	5.079	3.3	B_3
45	2.103	0.3	150	4.582	2.0	B_{11}
25	1.617	0.2	87	3.221	2.3	B_{312}

TABLE 1. Nusselt numbers calculated by the Galerkin continuation method at $Pr = 0.71$ and the relative difference, Δ, with respect to the Nusselt number obtained by a finite-difference solver for stable flow patterns.

$Ra/10^3$	Nu	$\Delta(\%)$	$Ra/10^3$	Nu	$\Delta(\%)$	Flow pattern
57	2.963	1.2	150	4.689	2.9	B_1
80	3.120	1.1	150	4.241	2.3	B_2
79	3.402	2.1	150	4.484	2.9	B_3
95	3.750	1.7	150	4.546	2.5	B_5
67.72	2.822	0.6	112	3.461	1.5	B_{24}
86	3.245	1.2				B_{25}
113	3.727	2.0	150	4.234	2.3	B_{26}
80	3.425	1.8	94	3.732	3.1	B_{34}
90	3.301	1.3	150	4.212	2.2	B_{251}

TABLE 2. As in table 1 but for $Pr = 130$.

with

$$f_j = \sum_i (L_{ji}(Ra)c_i) - Ra^{1/2}\sum_{i,n}(Q_{jin}(Pr)c_i c_n), \qquad j = 1, \cdots, N. \qquad (2.7b)$$

The components c_i of the vector $\boldsymbol{c}$ in (2.7b) are the unknowns, and the matrices with components L_{ji} and Q_{jin} contain the coefficients of the linear and nonlinear terms, respectively (see Puigjaner *et al.* 2004).

Bifurcations and stability of steady flow patterns have been mostly determined as a function of Ra for a fixed value of the Prandtl number. Provided that at least one solution of (2.7a) had been determined, an arclength continuation method was applied to calculate further solutions on the branch, until either $Ra = 1.5 \times 10^5$ was reached or the branch connected with another solution branch. The eigenvalue problem associated with the asymptotic stability of steady solutions along the different solution branches in the bifurcation diagram was solved. The twenty most unstable eigenvalues were calculated by means of the ARPACK implementation (Lehoucq & Sorensen 1996) of the Arnoldi method (Morgan 1996). Further details about the numerical procedure are provided in Puigjaner *et al.* (2004) and Puigjaner (2005).

A bifurcation study in the two-dimensional (Ra, Pr^{-1}) parameter plane was also performed for the flow pattern initially characterized by four connected half-rolls. To this end the arclength continuation method described in Puigjaner (2005) and used in Puigjaner *et al.* (2004, 2006) was modified to allow the continuation parameter to be either Ra or Pr^{-1} while keeping the other parameter fixed. Then, starting from a known flow pattern, solutions over the surface defined by $\boldsymbol{f}(\boldsymbol{c}, Ra, Pr) = 0$ were tracked using the continuation method with either Ra or Pr^{-1} fixed. The solution surface was determined by interpolation of the computed solutions over a triangular grid. The inverse of the Prandtl number, Pr^{-1}, turned out to be a more suitable parameter than Pr, both in the continuation procedure and in the graphical

Catton (1970)	Mizushima & Matsuda (1997)	Leong *et al.* (1998)	Present study	Flow pattern
6 974	6 798	6 969 $\pm$ 144 7 058 $\pm$ 119	6 799	B_1 (*x* or *y*-roll)
–	8 437	–	8 353	B_4 (single toroid)
–	11 609	–	11 612	B_3 (four connected half-rolls)

TABLE 3. Comparison of primary bifurcation Rayleigh numbers reported in the literature (Catton 1970; Mizushima & Matsuda 1997; Leong *et al.* 1998) with the present predictions. The values reported by Leong *et al.* (1998) are experimental and include the 95% confidence limits of uncertainty.

Pr	Flow transition	$N_t = 5$	$N_t = 6$	$N_t = 7$	$N_t = 8$	$\Delta_{7-8}(\%)$
0.71	$B_1 \rightarrow B_{11}$	44 564.03	44 668.88	44 699.57	44 701.89	0.005
0.71	$B_3 \rightarrow B_{33}$	94 712.79	90 970.35	90 209.66	90 183.32	0.03
130	$B_3 \rightarrow B_{33}$	20 650.48	20 641.74	20 637.05	20 634.32	0.01
130	$B_5 \rightarrow B_{54}$	93 540.48	94 023.88	94 416.93	94 523.05	0.1

TABLE 4. Convergence of calculated Rayleigh numbers at which bifurcations from different convective flow patterns occur as a function of the truncation parameters $N_t = N_x = N_y = N_z$. The rightmost column includes the relative difference between $N_t = 7$ and $N_t = 8$.

representation of the solution surface. Note that the convective term is small compared to the diffusive term in (2.1 *a–d*) for $Pr^{-1} \rightarrow 0$. Hence the steady counterpart of these equations is almost linear when $Pr^{-1} \rightarrow 0$.

2.4. *Accuracy assessment*

Results obtained with the Galerkin method have been compared with numerical solutions obtained by using the same fourth-order finite-difference solver as in Puigjaner *et al.* (2006). The finite-difference calculations were initialized from the velocity and temperature fields given by the Galerkin-based continuation method at some discrete values of the Rayleigh number. The relative differences in Nusselt number between the Galerkin and the finite-difference solutions are listed in tables 1 and 2 for those solutions that are stable over certain Ra ranges within the domain studied at $Pr = 0.71$ and 130, respectively. The maximum difference in Nusselt number between the Galerkin and the finite-difference solutions is 3.3 % at $Ra = 1.5 \times 10^5$ and $Pr = 0.71$.

Table 3 shows that the first bifurcation for the transition from the motionless conductive state to the onset of convection is predicted at $Ra_c = 6 799$. The stable flow pattern that develops takes the form of an *x* or *y* single roll, denoted B_1. This bifurcation value, which is independent of Pr, is in good agreement with numerical (Catton 1970; Mizushima & Matsuda 1997) and experimental (Leong *et al.* 1998) values previously reported in the literature. Table 3 also shows that the present predictions for the Ra values at which second and third bifurcations from the conductive state occur, differ by 1% and 0.03%, respectively, from those reported by Mizushima & Matsuda (1997). These transitions, which are also independent of Pr, respectively yield the single toroid B_4 and the four connected half-rolls B_3.

Convergence of secondary bifurcation Rayleigh numbers with respect to the truncation parameters N_x, N_y and N_z in (2.3) is shown in table 4 for two flow transitions at each Prandtl number. This table shows that an increase from

$N_t = N_x = N_y = N_z = 7$ to $N_t = 8$ causes at most a 0.1 % change in the bifurcation values considered.

3. Results and discussion

Bifurcation diagrams at both $Pr = 0.71$ and 130 are presented first and the spatial configurations of stable flow patterns and their evolution as Ra is increased are discussed. The effect of sidewall conductance on heat transport characteristics, which might be the reason for the disagreement among different experimental results, is then analysed by comparing current results with those previously obtained when adiabatic lateral walls were assumed. This is followed by a comparison of current results with the experimental studies of Leong *et al.* (1999) at $Pr = 0.71$ and Pallarès *et al.* (2001) at $Pr = 130$. Finally, the dependence of the flow pattern of four connected half-rolls on both the Rayleigh and the Prandtl numbers is comprehensively analysed by performing a bifurcation study in the two-dimensional (Ra, Pr^{-1}) parameter plane.

3.1. *Bifurcation diagrams and flow patterns at* $Pr = 0.71$ *and* 130

Bifurcation diagrams display a scalar measure of the changes in the solutions of a set of equations as a function of one or more parameters. They are very useful to depict the domains of existence, stability character and branching of the multiple solutions that may coexist when parameters are changed. In particular, the coexistence of several stable solutions for some ranges of parameters may yield hysteresis in time-dependent calculations (or in physical experiments) when the parameters are increased or decreased stepwise. In the current section bifurcation diagrams depict the branches of steady flow patterns in the (Ra, Nu_h)-space for two fixed values of the Prandtl number ($Pr = 0.71$ and 130). The Nusselt numbers Nu_h and Nu_c are respectively the dimensionless convective heat transport coefficients at the hot bottom and cold top plates, which were calculated as

$$Nu_h = 1 - \int_{-0.5}^{0.5} \int_{-0.5}^{0.5} \frac{\partial \theta}{\partial z}(x, y, -0.5)\,dx\,dy\,, \qquad (3.1a)$$

$$Nu_c = 1 - \int_{-0.5}^{0.5} \int_{-0.5}^{0.5} \frac{\partial \theta}{\partial z}(x, y, 0.5)\,dx\,dy. \qquad (3.1b)$$

The heat transferred through the hot bottom plate, Nu_h, and through the cold top plate, Nu_c, may not be necessarily the same when perfectly conducting lateral walls are assumed, in contrast to the case of adiabatic lateral walls (Puigjaner *et al.* 2004, 2006). Any difference in these two Nu values balances the heat transferred through the lateral walls. However, both Nusselt numbers are equal when the flow pattern is invariant under symmetries that cause the net overall heat transfer rate of the sidewalls to be zero. The effect of sidewall conductance on heat transport characteristics is discussed in § 3.2.

Bifurcations from the conductive state, are referred to as *primary bifurcations* and the term *secondary bifurcations* refers to bifurcations from convective flow solutions. The solution branches depicted in the bifurcation diagrams discussed in this section have been initiated from solutions that set in at primary bifurcations. The values of Ra at which primary bifurcations are predicted, together with the corresponding flow patterns that develop, are listed in table 5 for values of Ra up to 3×10^4. Primary bifurcations with two different flow patterns correspond to double eigenvalues of the linearized problem. Since the symmetry properties of flow patterns are useful to

Ra	Flow pattern	Generators of the isotropy subgroup	Order of the isotropy subgroup	Brief description
6 798	B_1	$\mathbf{S}_y, -\mathbf{I}$	4	y-roll
	B_2	$\mathbf{S}_{d_-}, -\mathbf{I}$	4	diagonal roll
8 353	B_4	$\mathbf{S}_y, \mathbf{S}_{d_+}$	8	single toroid
11 612	B_3	$-\mathbf{S}_y, \mathbf{S}_{d_+}$	8	four connected half-rolls
14 770	B_5	$\mathbf{S}_y, -\mathbf{S}_{d_+}$	8	four connected half-rolls diagonally aligned
23 498	B_6	$\mathbf{S}_y, -\mathbf{I}$	4	six connected half-rolls
	B_7	$\mathbf{S}_{d_-}, -\mathbf{I}$	4	three diagonal rolls
27 746	B_8	$\mathbf{S}_y, \mathbf{S}_z, \mathbf{S}_{d_+}$	16	double toroid

TABLE 5. Primary bifurcation Rayleigh numbers and main features of the corresponding flow patterns that set in for $Ra < 3 \times 10^4$.

understand their spatial configuration, generators of the isotropy subgroups are also included in table 5. The brief descriptions of the flow patterns provided in table 5 are valid for both $Pr = 0.71$ and 130 and refer to their three-dimensional spatial configuration at values of Ra close to the primary bifurcation value at which they set in.

The eigenfunctions of the linear problem at the first five primary bifurcation points listed in table 5 are similar to those reported by Bergeon, Henry & Knobloch (2001) for the three-dimensional Marangoni–Bénard convection problem in a cubical cavity. However, whereas the symmetry group associated with the current problem is $D_{4h} = Z_2 \times D_4$, the problem studied by Bergeon *et al.* (2001) has the dihedral group D_4 in $\mathbb{R}^2$ as a symmetry group. Consequently, the current eigenfunctions and the corresponding nonlinear flow patterns B_1, B_2, B_4, B_3 and B_5 involve additional symmetries.

The present study deals with stable flow patterns because the unstable ones are experimentally unattainable. However, initially unstable flow patterns were also considered because they can become stable as a consequence of subsequent bifurcations. Only those convective flow patterns having at most three (two) unstable eigenvalues near the primary (secondary) bifurcation point where they set in were tracked using the continuation method because the number of steady bifurcations was too large to continue all the solution branches emerging from identified bifurcations. In addition, when a solution branch ended at a bifurcation point of a different solution branch, the latter branch was also continued independently of the number of unstable eigenvalues of the affected flow pattern.

Summaries of all identified flow patterns at both $Pr = 0.71$ and 130 are presented in figures 1 and 2, respectively. In these figures, those flow patterns that are stable over certain ranges of Ra are printed in boldface. In addition, solutions that represent the same flow pattern, i.e. branches that in the bifurcation diagram connect two different bifurcation points, are joined by dashed arrows. The motionless conductive state is denoted C, convective flow patterns that set in at primary bifurcations are labelled B_i and flow patterns that develop at bifurcation values of B_i are denoted B_{ij}.

3.1.1. *Cavity filled with air (Pr = 0.71)*

The bifurcation diagram at $Pr = 0.71$ is depicted in figure 3. For the sake of clarity continued solutions that set in at secondary bifurcations and are unstable over the whole domain studied are not included in the bifurcation diagram unless they are
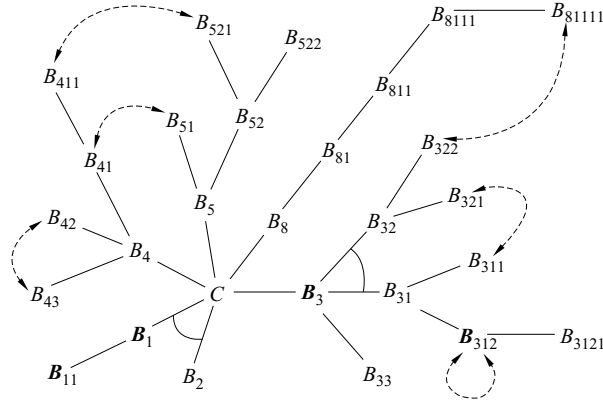
FIGURE 1. Sketch of the bifurcation diagram at $Pr = 0.71$. Solutions that are connected by a dashed arrow represent the same flow pattern. Solutions that set in at the same bifurcation point are joined with a solid arc. Flow patterns printed in boldface are stable over certain ranges of Rayleigh numbers in the region $Ra \leqslant 1.5 \times 10^5$. Note that the sketch only includes flow patterns that have been continued according to the criterion defined in §3.1.
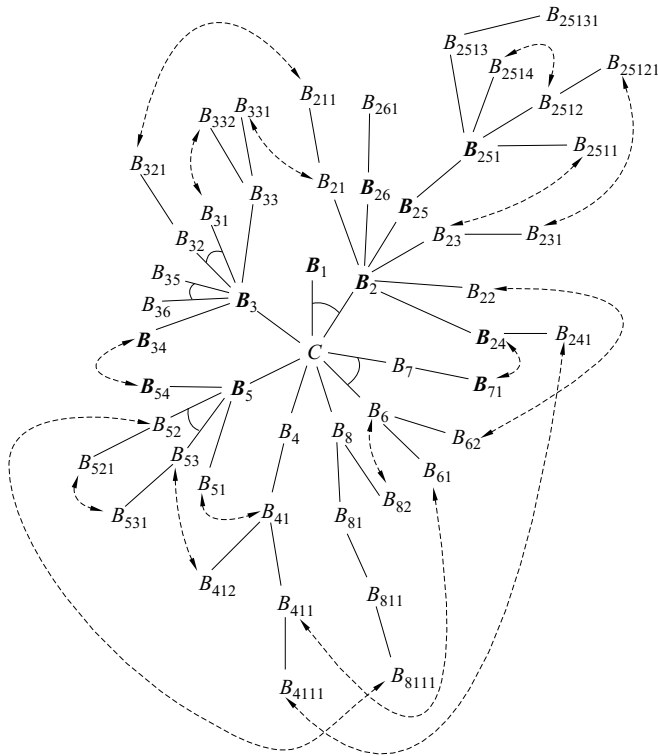
FIGURE 2. As in figure 1 but for $Pr = 130$.

needed to understand the origin of a stable solution. Figures 1 and 3 show that there are four steady flow patterns, denoted B_1, B_3, B_{11} and B_{312}, which are stable over certain ranges of Rayleigh number for $Ra \leqslant 1.5 \times 10^5$. The ranges of Ra where these solutions exist and the ranges of Ra where they are stable are summarized in table 6.

Flow pattern	Range of existence	Range of stability	Generators of the isotropy subgroup	Order of the isotropy subgroup	Topology shown in figures
B_1	6 798–	6 798–44 700	$\mathbf{S}_y, -\mathbf{I}$	4	5
B_{11}	44 700–	44 700–88 205	$\mathbf{S}_y$	2	6
B_3	11 612–	90 210–	$-\mathbf{S}_y, \mathbf{S}_{d_+}$	8	7 and 8
B_{312}	22 575–87 481	22 575–69 452	$\mathbf{S}_{d_+}, \mathbf{S}_{d_-}$	4	9

TABLE 6. Summary of the ranges of existence and stability, and symmetry properties of solutions that are stable over certain ranges of the Rayleigh number in the region $Ra < 1.5 \times 10^5$ at $Pr = 0.71$. $\mathbf{S}_y$, $\mathbf{S}_{d_+}$, $\mathbf{S}_{d_-}$, $-\mathbf{S}_y$ and $-\mathbf{I}$ are matrix representations of elements of the groups of symmetries.

Generators of the isotropy subgroup associated with each solution are also included in this table.

Table 6 shows that no stable steady solutions exist within the region $88\,205 \leqslant Ra \leqslant 90\,210$ at $Pr = 0.71$. Direct numerical simulations performed with an explicit time-marching finite-difference solver (see Puigjaner *et al.* 2004) reveal that the time evolution of the flow patterns is dependent on initial conditions over this region. For example, for intermediate Rayleigh numbers in the range $88\,205 \leqslant Ra \leqslant 90\,210$, the flow evolves towards a time-periodic solution when the B_{11} flow pattern is used as initial condition, while it presents a chaotic behaviour when it is initiated with a motionless field and a linear temperature distribution in z. The existence of a time-periodic solution is consistent with the destabilization of the B_{11} flow pattern through the supercritical Hopf bifurcation shown in figure 3(a). On the other hand, an examination of the chaotic time evolution shows that the flow approaches, at different times, two different unstable steady solutions and up to five different periodic solutions, all of them unstable. This chaotic behaviour suggests that connections between unstable and stable invariant manifolds of different unstable solutions (heteroclinic connections) occur. Moreover, these heteroclinic connections may, in turn, yield homoclinic connections, i.e. connections between the stable and the unstable manifold of the same solution. Future research will be directed towards the calculation of both unstable periodic solutions by using, for example, the Newton–Krylov approach (Sánchez *et al.* 2004), and invariant manifolds that yield heteroclinic and homoclinic connections (Simó 1990).

As discussed in §2.4, the onset of convection is predicted at the critical value $Ra_c = 6\,799$. Previous numerical studies (Catton 1970; Mizushima & Matsuda 1997) did not take into account that the critical value corresponds to a double eigenvalue of the linear problem whose associated linear independent eigenvectors take the form of one x-roll and one y-roll, respectively. Consequently, they predicted that the flow pattern developed at the onset of convection was of the x- or y-roll type. However, the equivariant singular theory (see Golubitsky, Stewart & Schaeffer 1988; Crawford & Knobloch 1991) predicts that in the generic case two types of solutions (modulo symmetry related solutions) must emerge simultaneously at this double bifurcation point. In the current study these two types of solutions were identified and denoted B_1 and B_2. B_1 and B_2 correspond respectively to the $\mathbf{S}_y$ and $\mathbf{S}_{d_-}$ symmetric solutions predicted by the theory. Figure 3(a) shows that both the B_1 and the B_2 solution branches are supercritical. This figure also shows that they are respectively stable and unstable when they set in, in agreement with the theory that predicts that only one of the two solutions can be stable when both are supercritical.
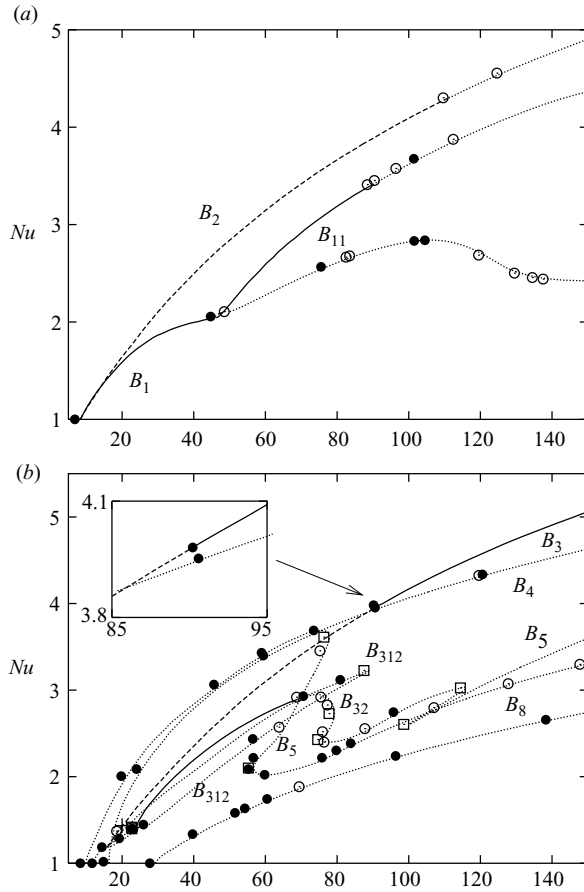
FIGURE 3. (*a*, *b*) For caption see facing page.

The method proposed by Jeong & Hussain (1995) to identify vortical structures has been used to characterize the spatial configuration of flow patterns. These authors identify a vortex core as the connected region of negative λ_2, being λ_2 the second largest eigenvalue of $\mathbf{S}^2 + \mathbf{\Omega}^2$, the sum of the squared symmetric and antisymmetric parts of the velocity gradient tensor. Passive tracer trajectories have been added in some cases to clarify the flow structure. It is worth mentioning that particles generally follow chaotic paths despite the steady nature of the solutions. However, a quasi-periodic behaviour is observed, with paths located on the surface of a torus, for values of Ra slightly above a primary bifurcation point.

The surfaces $\lambda_2 = 0$ depicted in figure 4 for the B_1 and B_2 flow patterns at $Ra = 7000$ show that both present a single-roll spatial configuration when they set in. The single roll is aligned along the y-axis in B_1 or in the positive diagonal direction in B_2. Figure 3(*a*) shows that the initially stable B_1 solution becomes unstable due to a symmetry-breaking bifurcation that occurs at $Ra = 44\,700$ whereas the B_2 flow pattern is unstable over the whole range of Ra investigated. Figure 5 shows that the B_1 solution still keeps the characteristic y-roll configuration at $Ra = 4.4 \times 10^4$ but it has developed vortical structures parallel to two diagonally opposite edges of the cavity.
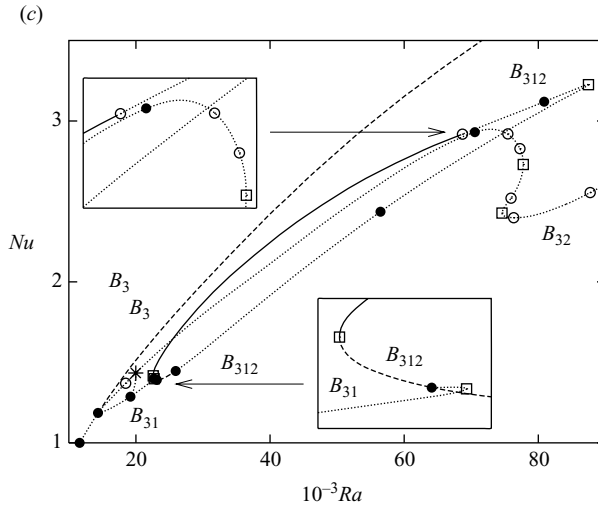
FIGURE 3. (*a–b*) Bifurcation diagram at $Pr = 0.71$. For clarity the bifurcation diagram is presented in two plots and additional close-ups of smaller domains are included. Stable flow patterns are depicted with solid lines; and unstable flow patterns by dashed lines when they have exactly one unstable eigenmode and by dotted lines when they have two or more unstable eigenmodes. Supercritical steady bifurcations, subcritical steady bifurcations, Hopf bifurcations and turning points are represented by filled circles, stars, hollow circles and hollow squares, respectively. (*a*) Flow patterns B_1, B_2 and B_{11}. (*b*) Flow patterns B_3, B_4, B_5, B_8, B_{31}, B_{32}, B_{311} and B_{312}. (*c*) Enlargement of the bifurcation diagram depicted in (*b*) for the flow patterns B_3, B_{31}, B_{32}, B_{311} and B_{312} at values of Ra within the range $5\,000 \leqslant Ra \leqslant 90\,000$.
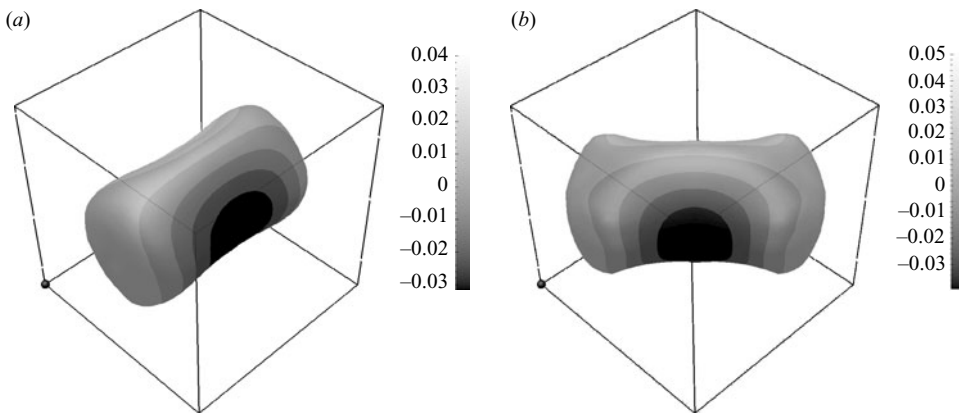
FIGURE 4. Surface of $\lambda_2 = 0$ for (*a*) the stable B_1 flow pattern and (*b*) the unstable B_2 flow pattern at $Ra = 7 \times 10^3$. Here and in all subsequent plots of $\lambda_2 = 0$ surfaces, the grey levels are scaled with the value of the vertical velocity component and the filled circle denotes the vertex with coordinates $(-0.5, -0.5, -0.5)$ while the coordinates of the lower frontal vertex are $(0.5, -0.5, -0.5)$.

An initially stable flow pattern, denoted B_{11} (see figure 3*a*), develops at the bifurcation point where the B_1 solution becomes unstable. This symmetry-breaking bifurcation is analogous to those previously reported by Puigjaner *et al.* (2004, 2006). The spatial configuration of the B_{11} flow pattern is initially sets in similar to that of the stable solution B_1 plotted in figure 5, except for the loss of the central symmetry,
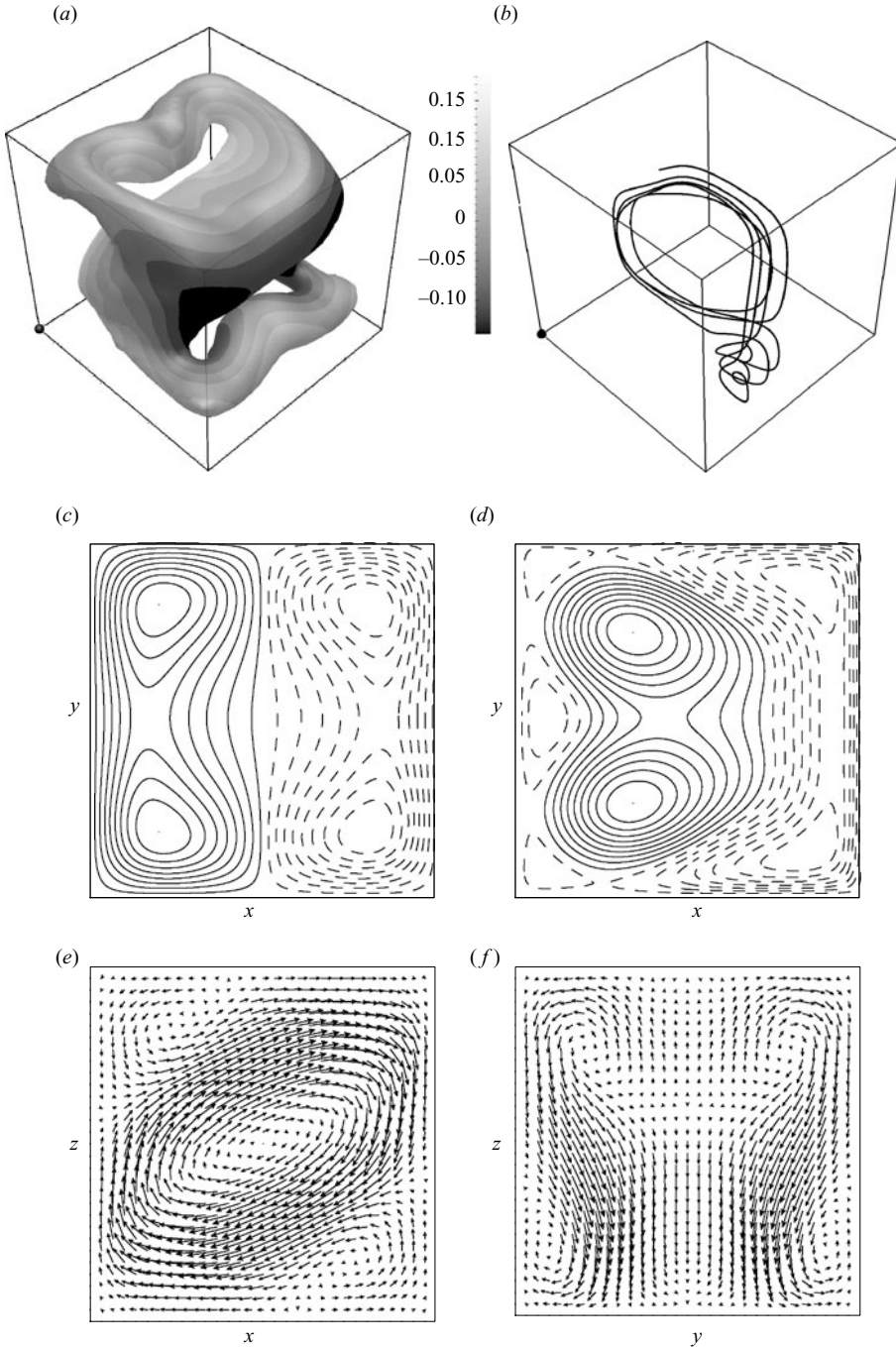
FIGURE 5. Stable B_1 flow pattern at $Ra = 4.4 \times 10^4$ and $Pr = 0.71$. (*a*) Surface of $\lambda_2 = 0$. (*b*) Passive tracer trajectory. (*c*, *d*) Vertical velocity contours at horizontal planes (*c*) $z = 0$ and (*d*) $z = 0.25$. Here and in all subsequent velocity contours plots, positive and negative values of the velocity are plotted with solid and dashed lines, respectively. (*e*, *f*) Projected velocity vectors at vertical planes (*e*) $y = 0$ and (*f*) $x = 0.125$.

(*a*)

(*b*)

(*c*)

(*d*)
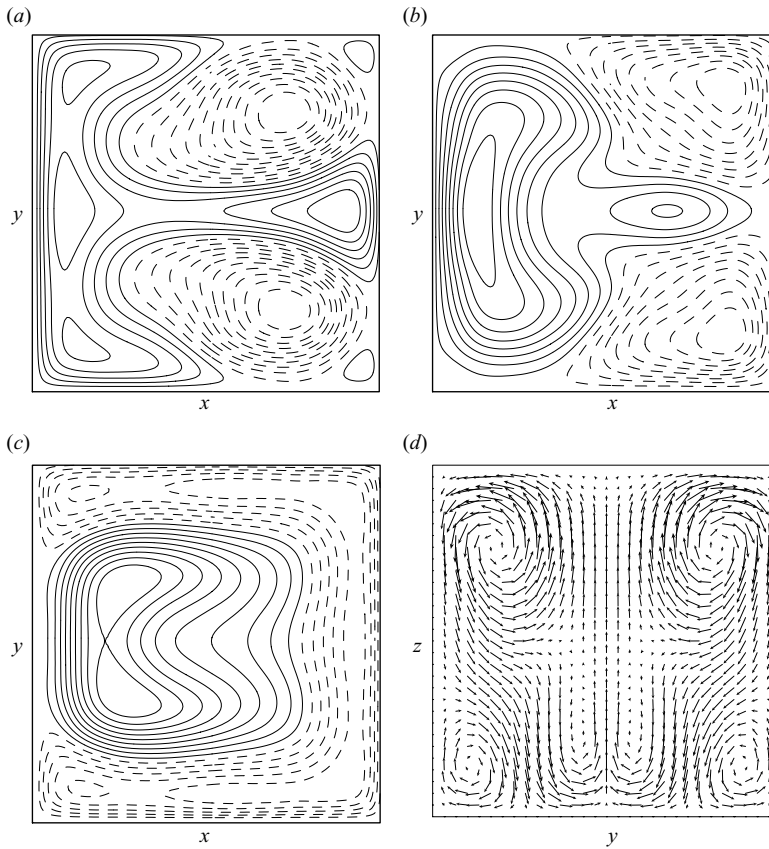
FIGURE 6. Stable B_{11} flow pattern at $Ra = 8.8 \times 10^4$ and $Pr = 0.71$. (*a–c*) Vertical velocity contours at horizontal planes (*a*) $z = -0.25$, (*b*) $z = 0$ and (*c*) $z = 0.25$. (*d*) Projected velocity vectors at the vertical plane $x = 0$.

denoted as $-I$ in table 6. However, figure 6 shows that the spatial configuration of the B_{11} flow pattern becomes more complex as Ra is increased. Whereas a y-roll configuration with a superposition of two relatively strong secondary vortical structures is adopted by B_{11} at the lower half of the cavity (figure 6*a*), the flow at the upper half presents a toroidal configuration (figure 6*c*) with air rising through the central part and sinking near the lateral walls, with a stronger downwelling motion near the lateral wall $x = 0.5$. The B_{11} flow pattern becomes unstable at $Ra = 88\,205$ as a consequence of a supercritical Hopf bifurcation, as shown in figure 3(*a*).

Figure 3(*b*) shows that the single toroidal flow pattern denoted B_4 that develops at the second primary bifurcation turns out to be unstable over the whole region investigated. An initially unstable flow pattern denoted B_3 sets in at the third primary bifurcation $Ra = 11\,612$ (see table 3 and figure 3*b,c*). Note that for adiabatic sidewalls the B_3 and B_4 flow patterns develop at the second and third primary bifurcation, respectively. Figure 7 shows that the B_3 flow pattern can be understood as four connected half-rolls at values of Ra slightly above the bifurcation point. As the Rayleigh number is increased secondary vortical structures parallel to the horizontal edges of the cavity are superimposed onto the characteristic four-half-roll configuration of the B_3 solution, as shown in figure 8. The B_3 flow pattern becomes

(a)

(b)
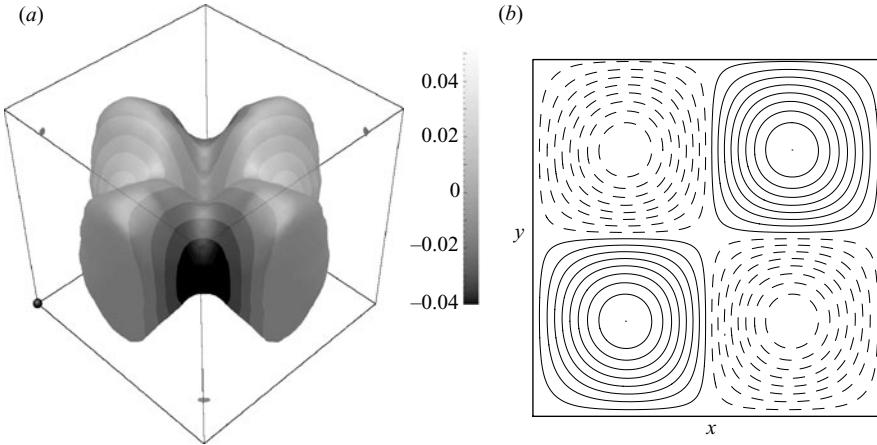
FIGURE 7. Unstable B_3 flow pattern at $Ra = 1.2 \times 10^4$ and $Pr = 0.71$. (a) Surface of $\lambda_2 = 0$. (b) Vertical velocity contours at the horizontal midplane $z = 0$.

(a)

(b)

(c)

(d)

(e)
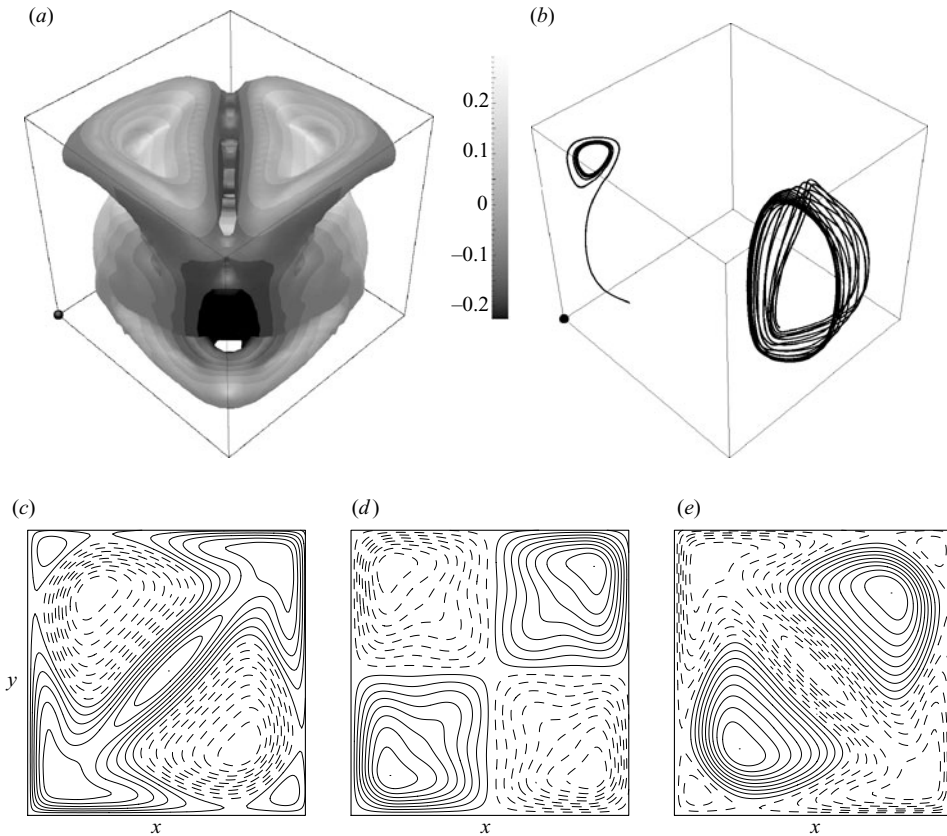
FIGURE 8. Stable B_3 flow pattern at $Ra = 1.5 \times 10^5$ and $Pr = 0.71$. (a) Surface of $\lambda_2 = 0$. (b) Passive tracer trajectories. (c–e) Vertical velocity contours at horizontal planes (c) $z = -0.25$, (d) $z = 0$ and (e) $z = 0.25$.

stable at $Ra = 90\,210$ and remains so thereafter, as shown in figure 3(b). Two of the three positive eigenvalues associated with the B_3 solution become negative at a double bifurcation point which takes place at $Ra = 14\,350$. At this bifurcation point

(*a*)

(*b*)

(*c*)

(*d*)
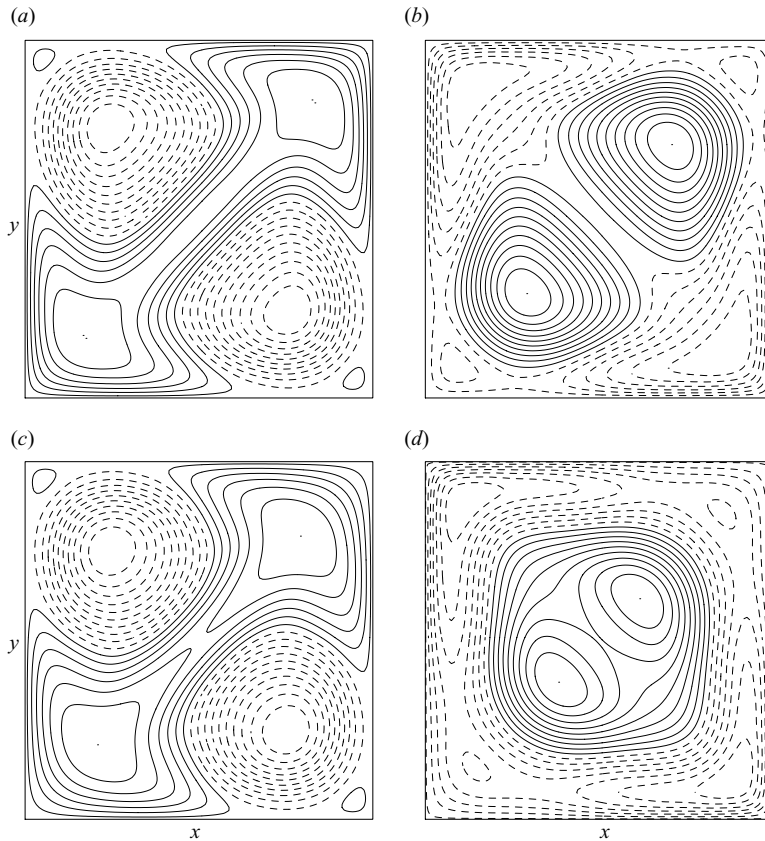
FIGURE 9. B_{312} flow pattern at $Ra = 5 \times 10^4$ and $Pr = 0.71$. (*a, b*) Vertical velocity contours of the stable B_{312} flow pattern (upper branch in the bifurcation diagram) at horizontal planes (*a*) $z = -0.25$ and (*b*) $z = 0.25$. (*c, d*) Vertical velocity contours of the unstable B_{312} flow pattern (lower branch in the bifurcation diagram) at horizontal planes (*c*) $z = -0.25$ and (*d*) $z = 0.25$.

two additional unstable flow patterns denoted B_{31} and B_{32} arise. The B_{31} and B_{32} flow patterns are invariant under $\boldsymbol{S}_{d_+}$ and $-\boldsymbol{S}_y$, respectively, in agreement with the theory (see Golubitsky *et al.* 1988). Figure 3(*c*) shows that the $-\boldsymbol{S}_y$ invariant flow pattern B_{31} connects the initially unstable B_3 solution with the solution denoted as B_{312}. One of the two realizations of the B_{312} solution (the upper branch in figure 3*c*) is stable over the range $22\,575 \leqslant \mathrm{Ra} \leqslant 69\,452$. Note that the destabilization of B_{312} occurs through a supercritical Hopf bifurcation. Figure 9(*a, b*) shows that the stable realization of B_{312} at $Ra = 50\,000$ presents a spatial configuration similar to that of B_3 plotted in figure 8. However, table 6 shows that the isotropy subgroups of both flow patterns are different. The B_{312} flow pattern maintains both diagonal reflection symmetries $\boldsymbol{S}_{d_+}$ and $\boldsymbol{S}_{d_-}$ but it has lost the $-\boldsymbol{S}_y$ symmetry present in the isotropy subgroup of B_3. The loss of this symmetry is difficult to see at the upper stable branch of B_{312} shown in figure 9(*a, b*) but becomes evident at the lower unstable branch of B_{312} plotted in figure 9(*c, d*).

3.1.2. *Cavity filled with silicone oil (Pr = 130)*

The bifurcation diagram sketched in figure 2 shows that all solutions that set in at primary bifurcations, except for the single-roll B_1, are connected to each other
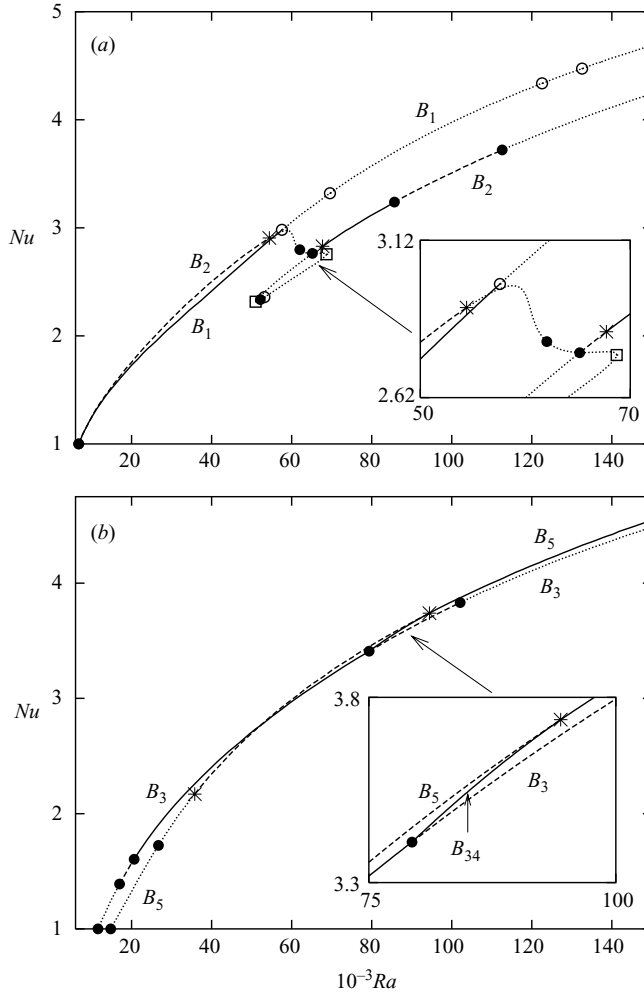
FIGURE 10. (*a*, *b*) For caption see facing page.

through their secondary bifurcations. For the sake of clarity the bifurcation diagram depicted in figure 10 includes only solution branches that are stable over certain ranges in the domain studied, and solutions that despite being unstable are necessary to understand the origin of stable ones. Figures 2 and 10 show that there are nine steady flow patterns, denoted B_1, B_2, B_3, B_5, B_{24}, B_{25}, B_{26}, B_{34} and B_{251}, which are stable over certain ranges of Ra in the region $Ra \leqslant 1.5 \times 10^5$. The ranges of Ra where these solutions exist, the ranges of Ra where they are stable and their isotropy subgroups are summarized in table 7.

Since primary bifurcations do not depend on the Prandtl number, solutions B_1, B_2, and B_3 correspond to the same flow structures previously discussed for $Pr = 0.71$ when they set in at primary bifurcations. However, their subsequent bifurcations and the evolution of their spatial configuration is rather different at $Pr = 130$. Figure 10(*a*) shows that the B_1 flow pattern is stable when it sets in at the onset of convection but it becomes unstable as a consequence of a supercritical Hopf bifurcation at $Ra = 57\,304$. Moreover, the B_1 solution does not present the symmetry-breaking bifurcation where the steady B_{11} flow pattern arises as observed for $Pr = 0.71$. Figure 11 shows that
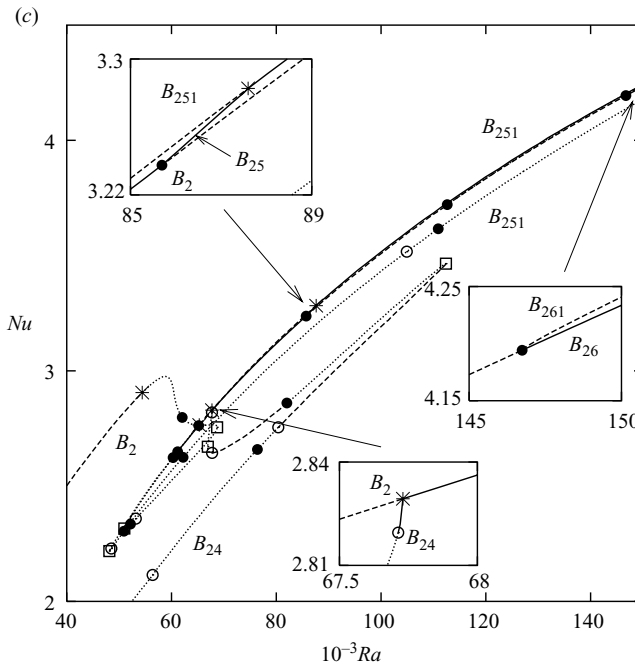
FIGURE 10. (*a–c*) Bifurcation diagram at $Pr = 130$. For clarity the bifurcation diagram is presented in three plots and additional zooms of smaller domains are included. See figure 3 for the notation. (*a*) Flow patterns B_1 and B_2. (*b*) Flow patterns B_3, B_5 and B_{34}. (*c*) Flow patterns B_2, B_{24}, B_{25}, B_{26} and B_{251} at values of Ra within the range $40\,000 \leqslant Ra \leqslant 150\,000$.

Flow pattern	Range of existence	Range of stability	Generators of the isotropy subgroup	Order of the isotropy subgroup	Topology shown in figures
B_1	6 798–	6 798–57 304	$\boldsymbol{S}_y, -\boldsymbol{I}$	4	11
B_2	6 798–	67 730–85 694	$\boldsymbol{S}_{d-}, -\boldsymbol{I}$	4	12
B_{24}	42 659–112 381	66 969–67 730	$\boldsymbol{S}_{d-}$	2	13(*a*)
B_{25}	85 694–87 598	85 694–87 598	$-\boldsymbol{I}$	2	
B_{251}	48 116–	61 160–65 297 87 598–	$\boldsymbol{S}_y, -\boldsymbol{I}$	4	14
B_{26}	112 622–	146 738–	$-\boldsymbol{S}_{d-}$	2	13(*b*)
B_3	11 612–	20 637–79 362	$-\boldsymbol{S}_y, \boldsymbol{S}_{d+}$	8	16
B_{34}	79 362–94 417	79 362–94 417	$-\boldsymbol{S}_y \cdot \boldsymbol{S}_{d+}$	4	18
B_5	14 770–	94 417–	$\boldsymbol{S}_y, -\boldsymbol{S}_{d+}$	8	15 and 17

TABLE 7. As in table 6 but for $Pr = 130$.

the B_1 flow pattern changes from a single roll to a double toroidal configuration at moderate values of Ra ($Ra = 5 \times 10^4$). Flow rises along the central part of the cavity and sinks near the lateral walls and vice versa at the upper and lower halves of the cavity, respectively, as shown in figure 11(*b,c*). Since B_1 is invariant under the central symmetry $-\boldsymbol{I}$ (see table 7) the upper toroid in figure 11(*a*) can be obtained from the lower one by applying this symmetry.

In contrast to the results obtained for $Pr = 0.71$, figure 10(*a,c*) shows that the initially unstable B_2 diagonal roll solution becomes stable at a subcritical bifurcation that occurs at $Ra = 67\,730$. The initially stable flow pattern developed at this
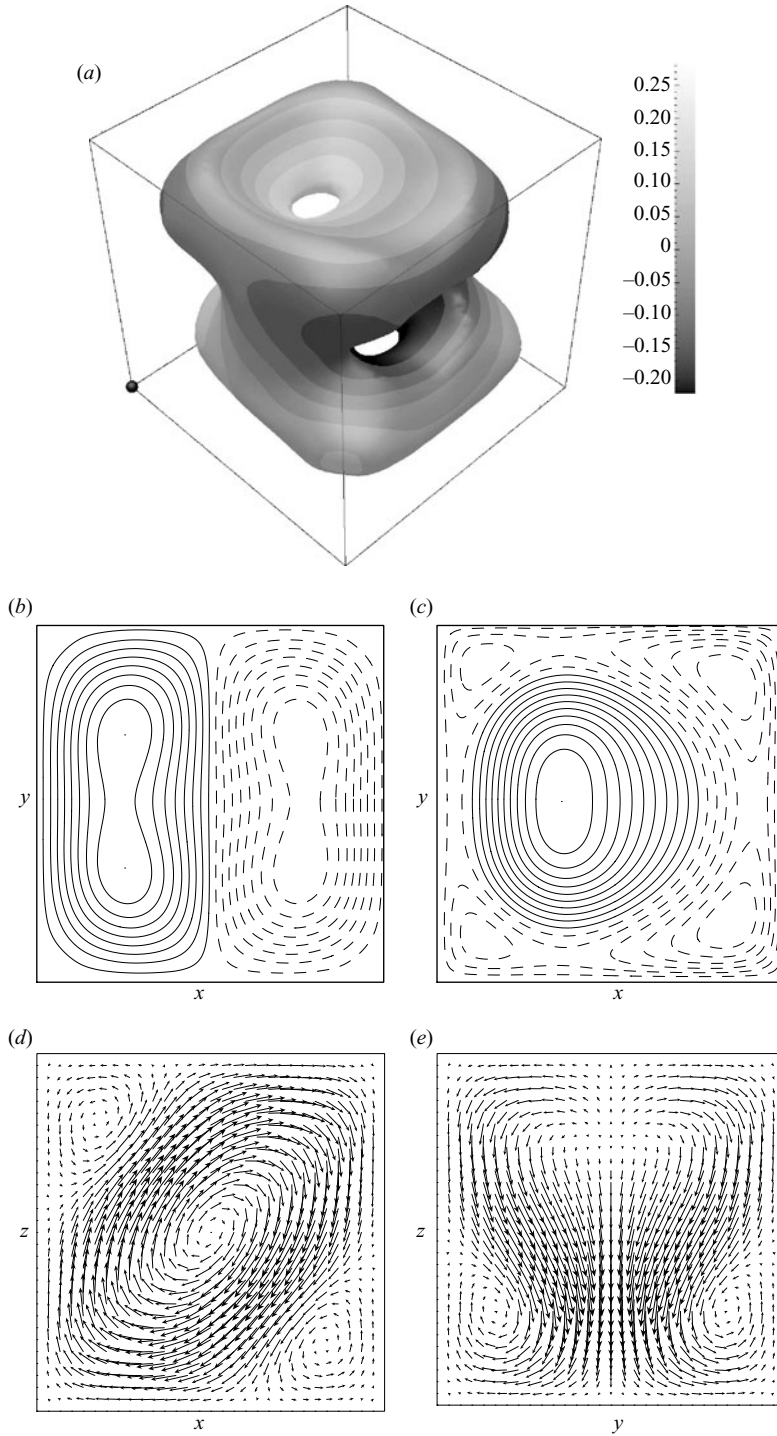
FIGURE 11. Stable B_1 flow pattern at $Ra = 5 \times 10^4$ and $Pr = 130$. (*a*) Surface of $\lambda_2 = 0$. (*b*, *c*) Vertical velocity contours at horizontal planes (*b*) $z = 0$, (*c*) $z = 0.25$ (*d*, *e*). Projected velocity vectors at vertical planes (*d*) $y = 0.25$ and (*e*) $x = 0.25$.
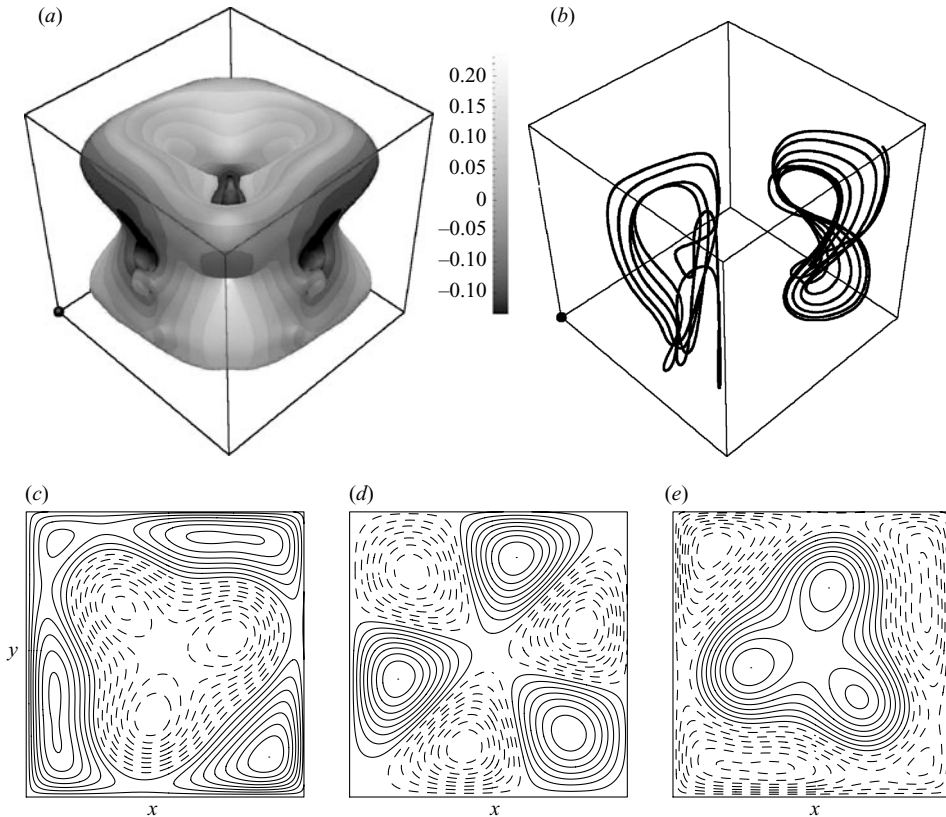
FIGURE 12. Stable B_2 flow pattern at $Ra = 8 \times 10^4$ and $Pr = 130$. (*a*) Surface of $\lambda_2 = 0$. (*b*) Passive tracer trajectories. (*c–e*) Vertical velocity contours at horizontal planes (*c*) $z = -0.25$, (*d*) $z = 0$ and (*e*) $z = 0.25$.

subcritical bifurcation point, denoted B_{24}, becomes unstable as a consequence of a subcritical Hopf bifurcation at $Ra = 66\,969$. Once the B_2 solution becomes stable it remains so until a new symmetry-breaking bifurcation takes place at $Ra = 85\,694$. Figure 10(*c*) shows that the stable flow pattern B_{25} that develops at this bifurcation connects the B_2 solution with the solution denoted B_{251}, causing a transfer of stability from the $\boldsymbol{S}_{d_-}$ invariant B_2 solution to the $\boldsymbol{S}_y$ invariant B_{251} solution. Figure 10(*c*) shows that this transfer of stability occurs without hysteresis. Since the B_{251} branch presents a turning point at $Ra = 48\,116$ two realizations of this flow pattern are possible for $Ra > 48\,116$. One of these realizations is stable over both regions $61\,160 \leqslant Ra \leqslant 65\,297$ and $Ra \geqslant 87\,598$. The B_{26} solution arises at the bifurcation point of B_2 that occurs at $Ra = 122\,622$ and it becomes stable at $Ra = 146\,738$, as shown in figure 10(*c*). Figure 12 shows that the B_2 solution at $Ra = 8 \times 10^4$ is no longer a diagonal roll, but, similarly to the B_1 solution discussed above (figure 11), it adopts a double toroidal configuration. Figures 13(*a*, *b*) and 14 show that the B_{24}, B_{26} and B_{251} flow patterns have similar spatial configurations to that discussed for the B_2 solution at $Ra = 8 \times 10^4$ (figure 12), despite of their different symmetry properties.

Figure 10(*b*) shows that the initially unstable flow pattern B_3 that sets in at the third primary bifurcation point ($Ra = 11\,612$) becomes stable at $Ra = 20\,637$ and remains
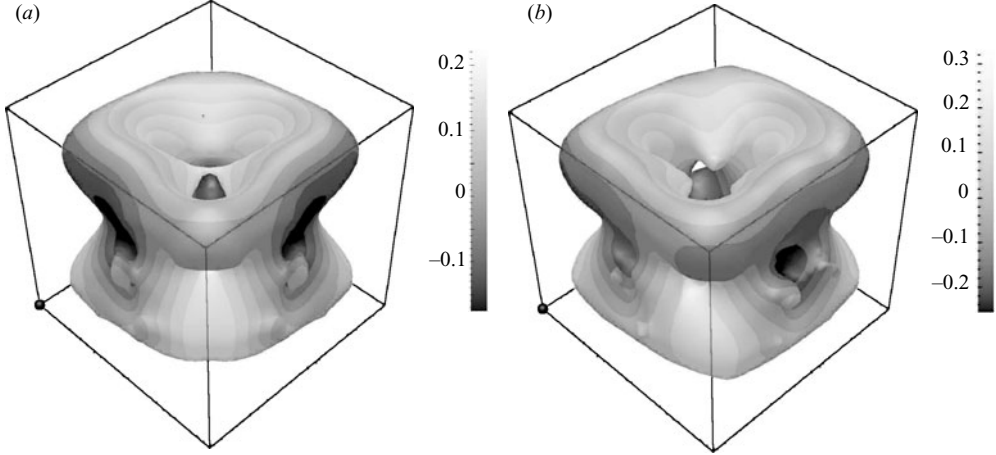
FIGURE 13. Surfaces of $\lambda_2 = 0$ at $Pr = 130$. (*a*) Stable B_{24} flow pattern at $Ra = 67\,720$.
(*b*) Stable B_{26} flow pattern at $Ra = 1.5 \times 10^5$.

so until a secondary bifurcation takes place at $Ra = 79\,362$. The bifurcations and stability regions of the B_3 flow pattern are discussed in more detail in §3.4.

The flow pattern B_5, which sets in as an initially unstable flow pattern at the fourth primary bifurcation point ($Ra = 14\,770$), becomes stable at $Ra = 94\,417$ and remains so thereafter (at least up to $Ra = 1.5 \times 10^5$), as shown in figure 10(*b*). Figure 15 shows that the B_5 flow pattern, at values of Ra slightly above the bifurcation point at which it originates, presents the configuration of four connected half-roll characteristic of the B_3 solution (see figure 7) but rotated an angle of $\pi/4$. Both the B_3 and the B_5 flow patterns evolve to a double toroidal configuration when Ra is increased, as shown respectively in figures 16 and 17 for $Ra = 1.5 \times 10^5$. Figure 10(*b*) shows that the stability of the B_3 and the B_5 solutions is transferred without hysteresis through the stable flow pattern denoted as B_{34}. The order of the isotropy subgroup of the B_{34} flow pattern is four, as shown in table 7, consistently with the symmetry-breaking bifurcations of the B_3 and the B_5 solutions. The isotropy subgroups of both flow patterns B_3 and B_5 are of order eight. This loss of symmetry is also evident in figure 18, where the configuration of the stable B_{34} flow pattern is depicted for $Ra = 8.7 \times 10^4$.

3.2. *Effect of sidewall conductance on heat transport characteristics*

The dimensionless rate of heat transfer from the hot bottom plate into the fluid, Nu_h, is equal to the rate of heat transferred between the fluid and the cold top plate, Nu_c, when the lateral walls are adiabatic. However, heat can also be transferred from the sidewalls into the fluid and vice versa when the lateral walls are conductive. In this case the two Nusselt numbers Nu_h and Nu_c may be different and differ from the total input heat transfer, which includes the heat transferred through the lateral walls. The total dimensionless input heat transfer, denoted Nu_t, is defined as

$$Nu_t = 1 + \left\langle \left(-\frac{\partial \theta}{\partial n} \cdot \boldsymbol{n} \right)^+ \right\rangle_{\partial D}, \qquad (3.2)$$

where $\langle (f)^+ \rangle_{\partial D}$ indicates an average of the positive values of f over the boundary surface of the domain D and $\boldsymbol{n}$ is the unit vector normal to the boundary surface.

To illustrate the differences in Nu figure 19 shows the variation of Nu_h, Nu_c and Nu_t with Ra for both the B_1 and the B_{11} flow patterns at $Pr = 0.71$. The central

(*a*)
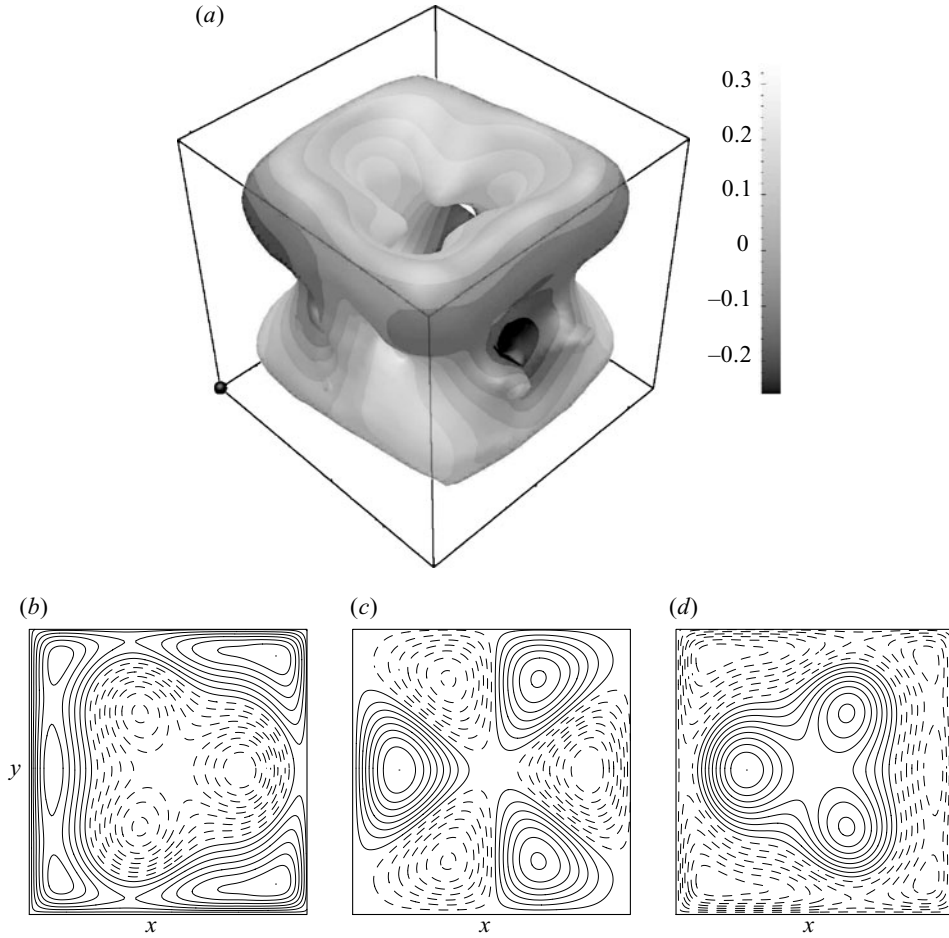
FIGURE 14. Stable B_{251} flow pattern at $Ra = 1.5 \times 10^5$ and $Pr = 130$. (*a*) Surface of $\lambda_2 = 0$. (*b*–*d*) Vertical velocity contours at horizontal planes (*b*) $z = -0.25$, (*c*) $z = 0$ and (*d*) $z = 0.25$.

(*a*)   (*b*)
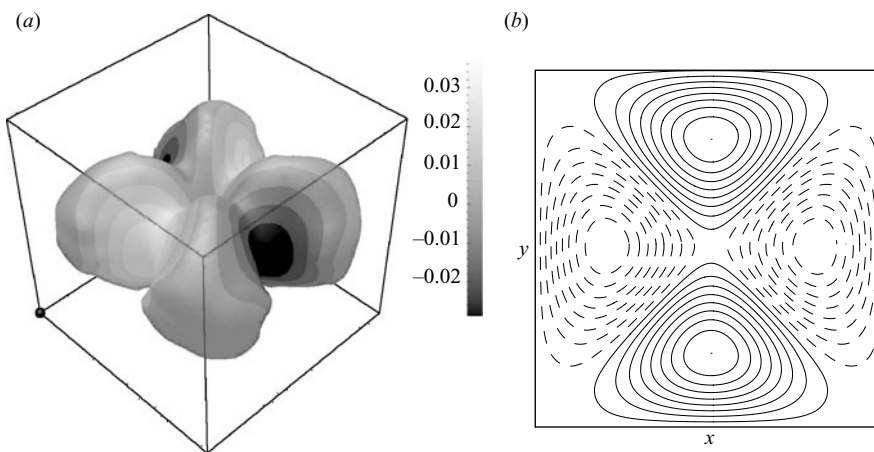
FIGURE 15. Unstable B_5 flow pattern at $Ra = 1.5 \times 10^4$ and $Pr = 130$. (*a*) Surface of $\lambda_2 = 0$. (*b*) Vertical velocity contours at the horizontal midplane $z = 0$.
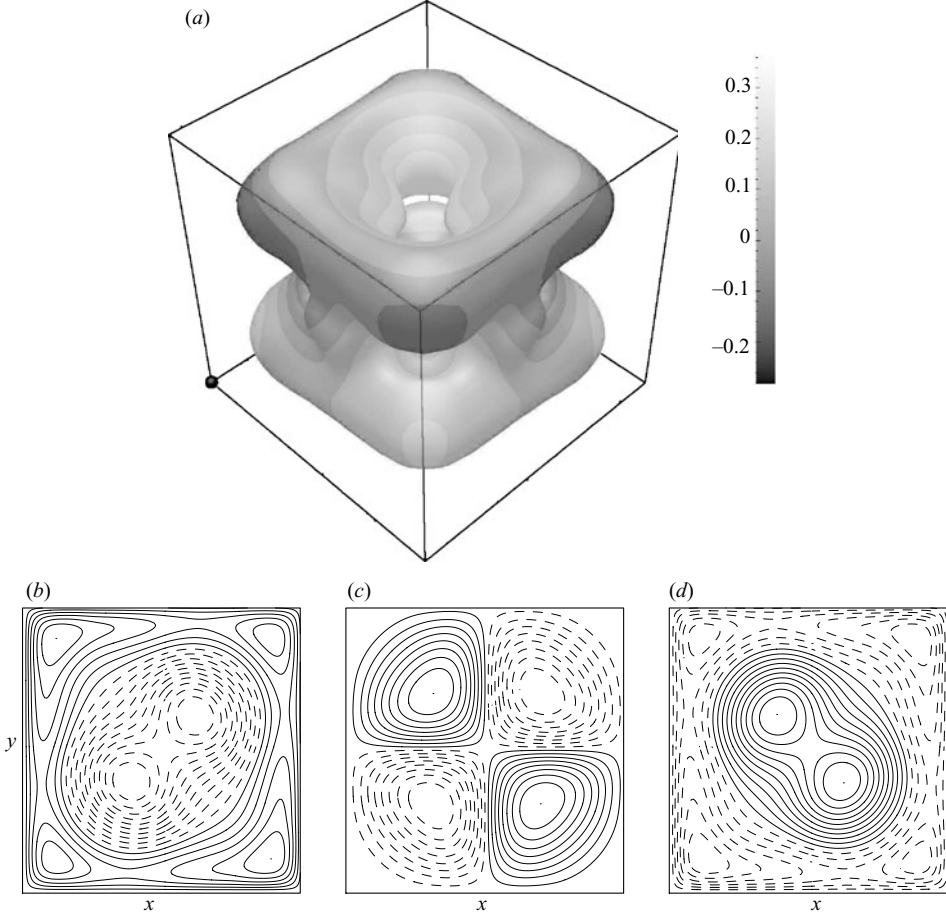
FIGURE 16. Unstable B_3 flow pattern at $Ra = 1.5 \times 10^5$ and $Pr = 130$. (*a*) Surface of $\lambda_2 = 0$. (*b–d*) Vertical velocity contours at horizontal planes (*b*) $z = -0.25$, (*c*) $z = 0$ and (*d*) $z = 0.25$.

symmetry of the B_1 flow pattern (see table 6) causes the net overall heat transfer rate of the sidewalls to be zero. As a consequence the values of Nu_h and Nu_c are equal for the B_1 flow pattern in figure 19. In contrast, the initially stable flow pattern B_{11} yields different Nu at the two horizontal bottom and top plates due to the loss of the central symmetry property; this difference balances the heat exchanged through the lateral walls. Figure 19 also shows the enhanced heat transfer ability of the B_{11} flow pattern compared to the B_1 solution. The Nu_t for B_{11} is always above the corresponding Nu_h and Nu_c values, indicating the contribution of sidewalls to the total heat transfer rate.

The sidewall effect can be quantified by comparing the present Nusselt numbers, Nu_h, Nu_c and Nu_t, with the Nusselt number at the bottom hot plate obtained when the adiabatic boundary condition is applied, which is denoted Nu_{ad}. Values of Nu_h, Nu_c, Nu_t and Nu_{ad} are reported in table 8 for the flow patterns B_1, B_{11}, B_2 and B_3 at several values of Ra for both $Pr = 0.71$ and 130. The factor $C = (Nu_h - Nu_{ad})/Nu_{ad}$, used by Verzicco (2002) to determine the effect of sidewall conductance on the heat transport in a cylindrical cavity, is also included in table 8. It is observed in this table that C is dependent on the particular flow pattern and has larger absolute values for those flow patterns whose spatial configurations differ more from the corresponding
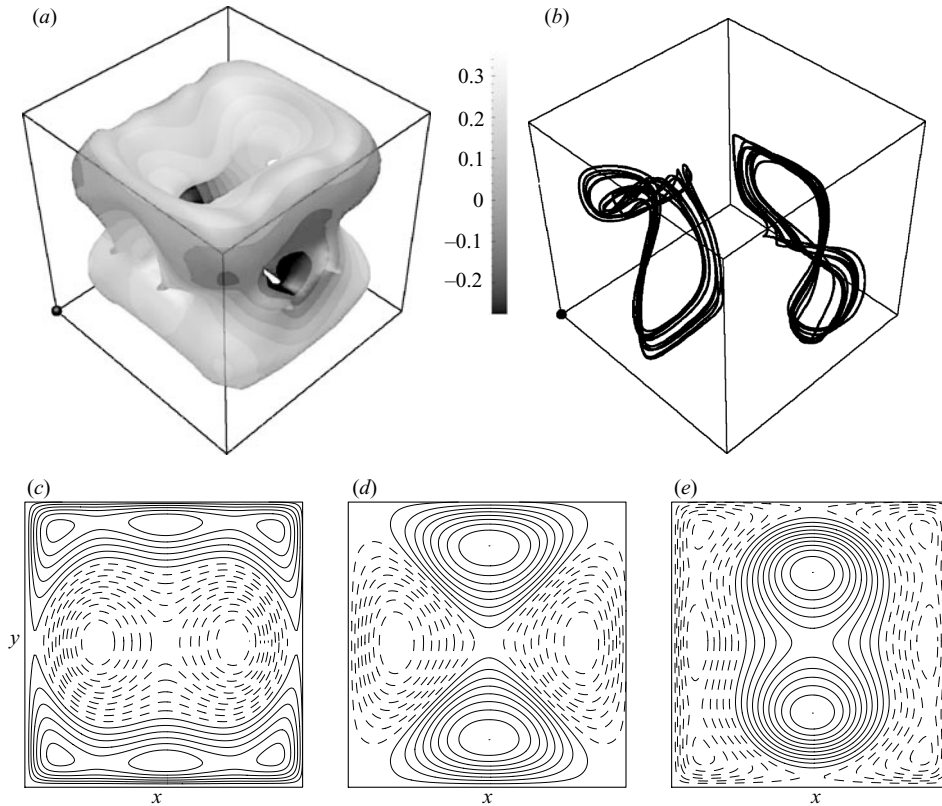
FIGURE 17. Stable B_5 flow pattern at $Ra = 1.5 \times 10^5$ and $Pr = 130$. (*a*) Surface of $\lambda_2 = 0$. (*b*) Passive tracer trajectories. (*c–e*) Vertical velocity contours at horizontal planes (*c*) $z = -0.25$, (*d*) $z = 0$ and (*e*) $z = 0.25$.

ones in the cavity with adiabatic lateral walls. Table 8 shows that the highest value of $|C| = 0.4$ is obtained in the case of the B_1 flow pattern at $Ra = 1.5 \times 10^5$ and $Pr = 0.71$. Note that the highest relative difference between Nu_t and Nu_h, denoted F in table 8, is also reached in this case, indicating that differences in the flow pattern configurations between adiabatic and perfectly conducting lateral walls condition the amount of heat transferred to the system through the lateral walls. Values of the quantity Nu_t/Nu_{ad}, listed in the rightmost column of table 8, indicate that, overall, flow patterns transfer heat more efficiently in the perfectly conducting case than they do in the adiabatic case.

3.3. *Comparison with experiments*

The present results can be compared with the experimental studies reported by Leong *et al.* (1999) and Pallarès *et al.* (2001). Both experiments were performed in a cubical cavity with lateral walls approximating perfectly conducting boundary conditions. The physical devices used in these experiments are sketched in figure 20. Air ($Pr = 0.71$) was used as fluid in the experiments of Leong *et al.* (1999), whereas the experimental cavity used by Pallarès *et al.* (2001) was filled with silicone oil ($Pr = 130$). Pallarès *et al.* (2001) used the dimensionless number $\gamma = k_f L/(k_w d_w)$ to quantify the finite thermal conductivity of the sidewalls. In this expression k_f and k_w are respectively the thermal conductivities of the fluid and the walls, d_w is the thickness of the lateral walls and L

D. Puigjaner, J. Herrero, C. Simó and F. Giralt
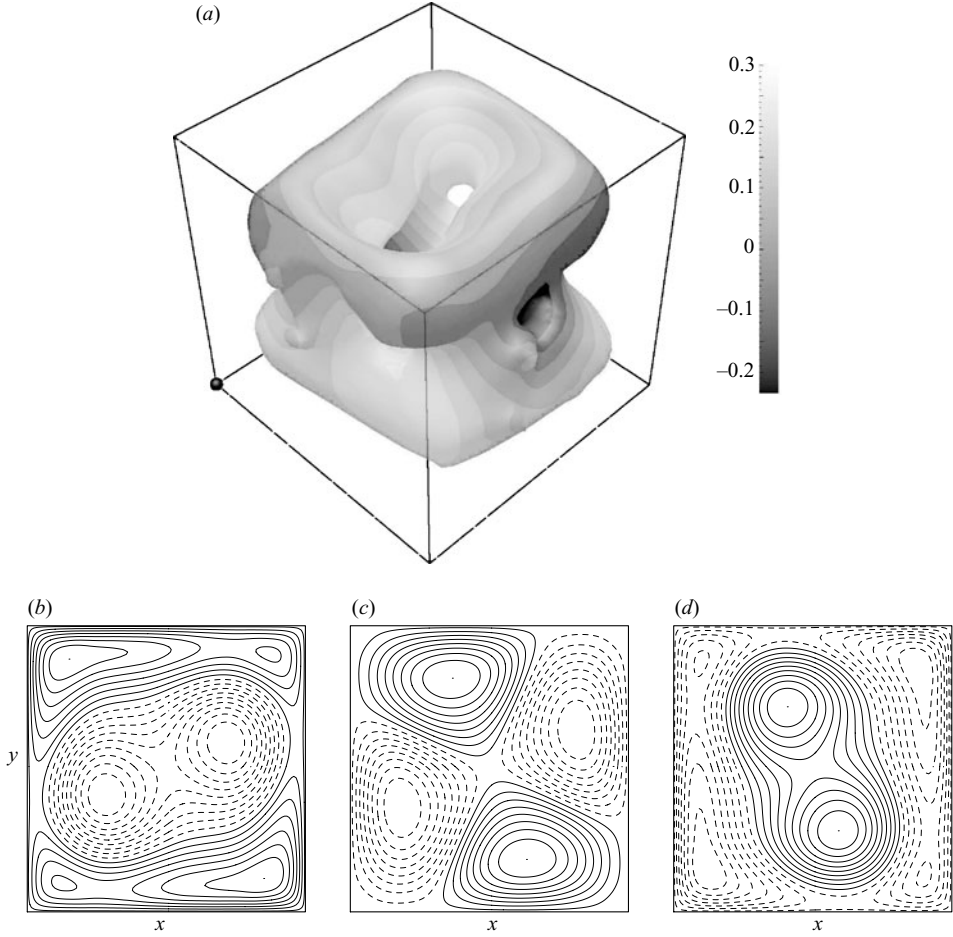
FIGURE 18. Stable B_{34} flow pattern at $Ra = 8.7 \times 10^4$ and $Pr = 130$. (*a*) Surface of $\lambda_2 = 0$.
(*b–d*) Vertical velocity contours at horizontal planes (*b*) $z = -0.25$, (*c*) $z = 0$ and (*d*) $z = 0.25$.

Flow pattern	$Ra/10^3$	Pr	Nu_h	Nu_t	Nu_{ad}	F	C	Nu_t/Nu_{ad}
B_1	50	0.71	2.13	3.27	3.07	0.35	−0.31	1.06
B_1	150	0.71	2.42	4.19	4.05	0.42	−0.40	1.03
B_1	50	130	2.74	3.62	3.10	0.24	−0.12	1.17
B_1	150	130	4.69	6.26	4.13	0.25	0.14	1.52
B_{11}	88	0.71	3.89 / 3.40	5.31	4.04	0.27 / 0.36	−0.04 / −0.16	1.31
B_{11}	150	0.71	4.58 / 4.37	6.18	5.10	0.26 / 0.29	−0.10 / −0.14	1.21
B_2	150	130	4.24	5.94	4.41	0.29	−0.04	1.35
B_3	150	0.71	5.08	7.43	5.41	0.32	−0.06	1.37
B_3	150	130	4.48	5.93	5.07	0.24	−0.12	1.17

TABLE 8. Comparison of the present heat transfer coefficients, Nu_h and Nu_t, with those reported
for adiabatic lateral walls, Nu_{ad}. The two possible Nu_h values, depending on the y-vorticity
sign, are included for the B_{11} flow pattern. $F = (Nu_t - Nu_h)/Nu_t$ and $C = (Nu_h - Nu_{ad})/Nu_{ad}$.
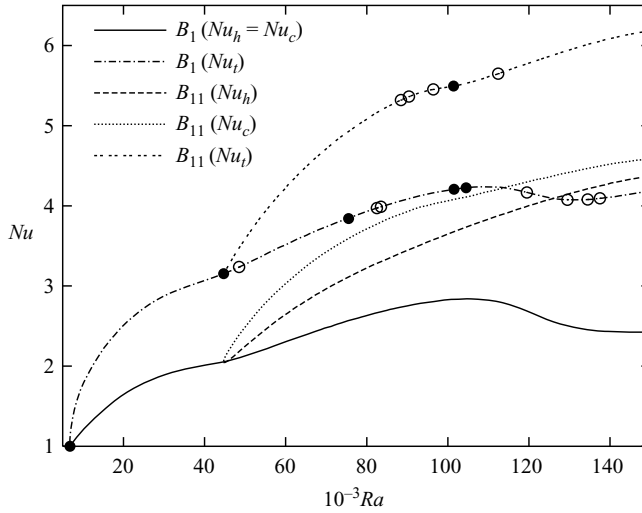
FIGURE 19. Variation of the Nusselt numbers Nu_h, Nu_c and Nu_t with Rayleigh number for the B_1 and B_{11} flow patterns at $Pr = 0.71$. Steady and Hopf bifurcations are represented with filled and hollow circles, respectively.
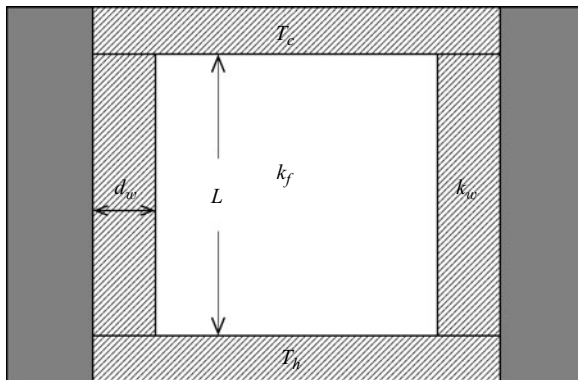
FIGURE 20. Sketch of a section of the physical device at $x = 0$. The hatched domains correspond to highly conductive walls. The bottom and top plates are kept at constant hot and cold temperatures T_h and T_c, respectively. The grey strips indicate that the lateral walls are insulated to prevent the lateral loss of heat from the device. Thermal conductivities of the fluid and the walls are k_f and k_w, respectively.

is the height of the cavity. The dimensionless number γ is equivalent to the inverse of the quantity denoted as W by Verzicco (2002). The value $\gamma = 0$ corresponds to perfectly conducting lateral walls. The values of γ corresponding to the experimental set-ups of Leong *et al.* (1999) and Pallarès *et al.* (2001) were respectively $\gamma = 0.0026$ $(L/d_w = 39.9, k_f/k_w = 6.5 \times 10^{-5})$ and $\gamma = 0.45$ $(L/d_w = 0.625, k_f/k_w = 0.72)$.

3.3.1. *Cavity filled with air ($Pr = 0.71$)*

Table 3 shows that the critical Rayleigh number predicted in the current study is in good agreement with the experimental value reported by Leong *et al.* (1999). Differences between current predictions and experimental Nusselt numbers are below 4 % in all cases, as shown in table 9. This table also includes the name of the

	Nu		
$Ra/10^3$	Present study	Leong *et al.* (1999)	Flow pattern
10	1.202	1.246 ± 0.013	B_1
40	2.008	2.018 ± 0.017	B_1
100	3.648	3.509 ± 0.035	B_{11}
100	4.062	3.916 ± 0.042	B_{11}

TABLE 9. Comparison of the cold-plate Nusselt numbers with experimental results reported by Leong *et al.* (1999). The rightmost column includes the corresponding flow pattern predicted in the current study.

corresponding flow pattern predicted by the Galerkin method. As discussed in §3.2 the B_{11} flow pattern yields different values of Nu_h and Nu_c. Thus, it may be possible that the two different values of Nu reported by Leong *et al.* (1999) at $Ra = 10^5$ (see table 9) correspond to two different particular elements in the orbit of the B_{11} solution that are related by the central symmetry $-I$. This explanation is consistent with the fact that Leong *et al.* (1999) reported that the Nu_c value of one solution coincided with the Nu_h value of the other and vice versa. These authors reported a steady flow pattern that resembles the current B_{11} at $Ra = 10^5$. This value of the Rayleigh number is only slightly higher than the $Ra = 88\,205$ value at which, according to the present results, the B_{11} flow pattern becomes unstable as a consequence of a supercritical Hopf bifurcation.

3.3.2. *Cavity filled with silicone oil (Pr = 130)*

The only flow patterns experimentally observed by Pallarès *et al.* (2001) for conducting lateral walls in the range $5 \times 10^3 \leqslant Ra \leqslant 8 \times 10^4$ were those denoted $S1$, $S2$ and $S5$ by these authors, which respectively correspond to the current B_1, B_2 and B_3 flow patterns. The unstable toroidal flow pattern B_4, which was denoted $S4$ by Pallarès *et al.* (2001), was experimentally identified in that work as a transitional state during the start-up of the experimental apparatus. This transitional B_4 flow pattern eventually evolved to the B_2 solution. Figure 21(*a*) shows the sequence of flow transitions from the B_2 solution to other steady flow patterns reported by Pallarès *et al.* (2001) when Ra was increased or decreased. As Ra was increased the first transition from the diagonal roll B_2 to the single roll B_1 was experimentally observed in the range $10^4 < Ra < 2 \times 10^4$. The second transition was observed in the range $5 \times 10^4 < Ra < 5.5 \times 10^4$ and B_1 evolved again towards the B_2 flow pattern. Finally, in the range $6 \times 10^4 < Ra < 6.5 \times 10^4$ a third transition from the B_2 solution to the B_3 flow pattern was experimentally identified. Once the B_3 flow pattern had developed, it remained stable on decreasing the Rayleigh number until the initial diagonal roll B_2 was recovered in the range $10^4 < Ra < 2 \times 10^4$. Furthermore, Pallarès *et al.* (2001) reported that a flow pattern, denoted $S6$ by those authors, developed at $Ra = 1.2 \times 10^5$ and remained stable when the Rayleigh number was decreased to $Ra = 8 \times 10^4$.

The present study predicts that both the initially stable B_1 and the initially unstable B_2 flow patterns develop at the smallest primary bifurcation ($Ra_c = 6\,798$). The current continuation method also predicts that the B_2 flow pattern remains unstable until a bifurcation takes place at $Ra = 67\,730$, as observed in figure 10. Figure 21(*a*) shows that the value of Ra at which the transition from the B_1 solution to the B_2 solution was experimentally observed agrees in figure 21(*b*) with the current predicted value of Ra where the B_1 solution becomes unstable. However, the experimentally observed
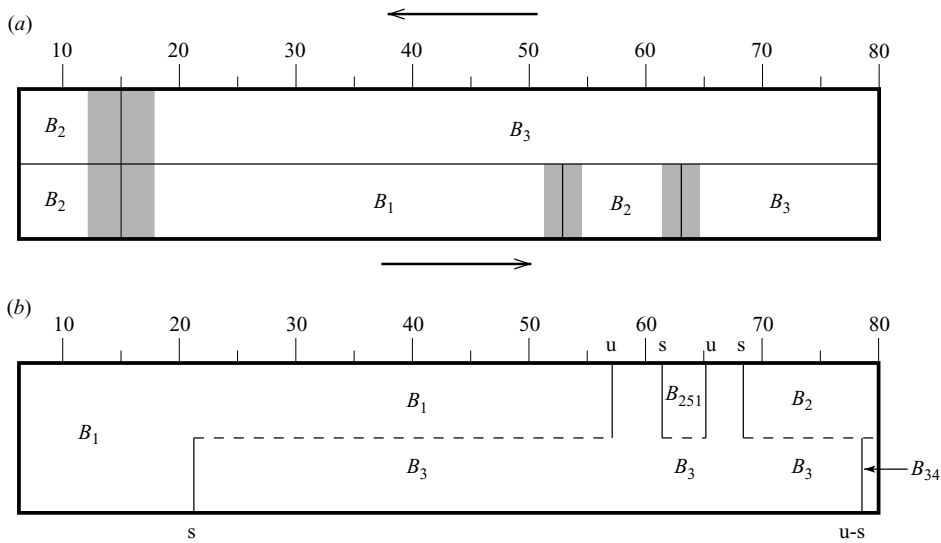
FIGURE 21. (*a*) Sequence of flow transitions from the conductive state observed experimentally by Pallarès *et al.* (2001) as Ra was increased and decreased stepwise (the experimental range of Ra where each transition was observed is indicated by grey strips). (*b*) Stable flow patterns identified by the current continuation method. Flow patterns printed above and below horizontal dashed lines are stable. Bifurcations are marked with vertical solid lines. Bifurcation points where a flow pattern becomes stable or unstable are respectively labelled with s or u. The label u-s indicates that the initially stable flow pattern B_{34} sets in at the bifurcation point where the B_3 solution becomes unstable.

consecutive transitions from B_1 to B_2 and from B_2 to B_3 flow patterns in figure 21(*a*) are not found in the current study (figure 21*b*) where the B_1 solution becomes unstable as a consequence of a Hopf bifurcation. Nevertheless, it is possible that the flow pattern found experimentally within the range $5.5 \times 10^4 \leqslant Ra \leqslant 6.5 \times 10^4$ was the B_{251} solution, which is predicted to be stable within the ranges $61\,160 \leqslant Ra \leqslant 65\,297$ and $Ra \geqslant 87\,598$, as shown in table 7. The spatial configuration of the B_{251} flow pattern at $Ra = 6.3 \times 10^4$ is rather similar to that plotted in figure 12 for the B_2 solution at $Ra = 8 \times 10^4$. The current study predicts that the B_3 solution becomes stable at $Ra = 20\,637$, which is consistent with the experimentally observed stability of this solution on decreasing the Rayleigh number to $Ra = 2 \times 10^4$. In addition, the spatial structure of the flow pattern B_5, shown in figure 15, and its region of stability ($Ra \geqslant 94\,417$), suggest that the solution denoted $S6$ by Pallarès *et al.* (2001) might correspond to the current B_5 flow pattern. This hypothesis is reinforced by the connection between the B_3 and the B_5 solutions in the bifurcation diagram depicted in figure 10(*b*).

The realizability of a stable flow pattern can be characterized by the measure of its basin of attraction in the space of initial perturbed states. Only those flow patterns whose basin of attraction overlaps with the initial conditions used in the experiment are experimentally attainable. Thus, it is unlikely that a flow pattern with a narrow stability domain, like B_{24}, would be found experimentally. On the other hand, imperfections in the experimental set-up may produce important changes in the bifurcation diagram, specially when these imperfections break some of the symmetries of the problem. When the diagonal symmetry is broken due to geometric imperfections, the splitting of double zero eigenvalues into primary and secondary
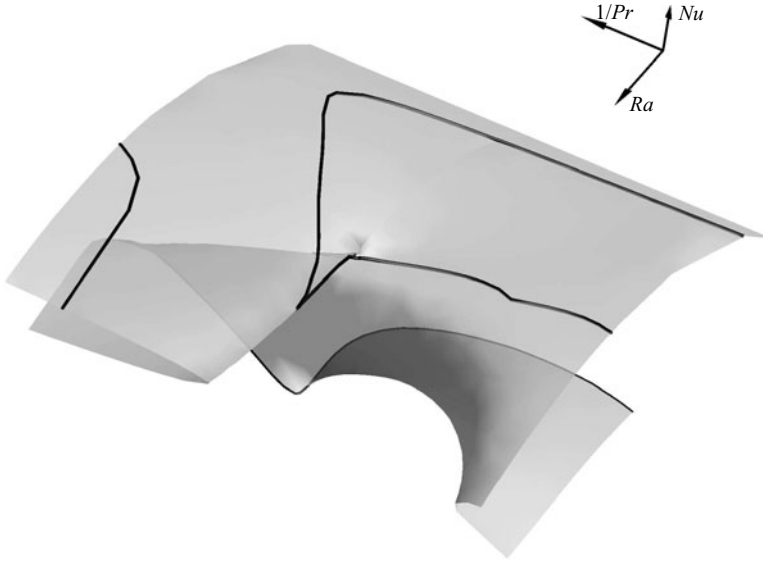
FIGURE 22. Variation of the Nusselt number with Rayleigh number and the inverse of the Prandtl number for the B_3 solution in the ranges $1.2 \times 10^4 \leqslant Ra \leqslant 1.2 \times 10^5$ and $0.71 \leqslant Pr \leqslant 130$. The bifurcation curves where the stability character of the B_3 solution changes are depicted as black solid lines over the solution surface.

bifurcations is expected. In particular, the critical bifurcation where the B_1 (x- or y-roll) and B_2 (diagonal roll) solutions emerge will split into two successive primary bifurcations, one producing an x-roll solution and the other a y-roll solution, when the cavity is slightly rectangular. Moreover, for a small enough departure from a square cross-section a secondary bifurcation on one of these roll branches will occur near the primary bifurcation. At this secondary bifurcation a flow pattern that resembles the diagonal roll B_2, but no longer with the S_{d_-} symmetry property, will set in (see Crawford & Knobloch 1988; Bergeon *et al.* 2001).

3.4. *Effect of the Prandtl number*

Comparison of the bifurcation diagrams for $Pr = 0.71$ and 130 respectively presented in figures 3 and 10 reveals that the evolution of flow patterns with Ra, their spatial configurations and stability character, and their subsequent bifurcations depend strongly on the Prandtl number. These differences are also evident in terms of regions of stability when tables 6 and 7 are compared, particularly for flow patterns B_2, B_3 and B_5. Both B_2 and B_5 are unstable over the whole region $Ra \leqslant 1.5 \times 10^5$ at $Pr = 0.71$, but they are stable over some ranges within the domain studied at $Pr = 130$.

The B_3 flow pattern, which is initially formed by four connected half-rolls, shows completely different regions of stability at $Pr = 0.71$ and 130, that deserve a more exhaustive bifurcation study in the two-dimensional (Ra, Pr) parameter plane. The three-dimensional surface plotted in figure 22 shows the variation of the Nusselt number for the B_3 solution as a function of the two control parameters Ra and Pr^{-1}. The presence of folds in this figure indicates that several realizations of the B_3 flow pattern are possible for some values of Ra and Pr^{-1}. The parameter chart plotted in figure 23 shows the regions where different number of flow realizations, varying from zero to five, are possible. The dashed curve from a to b in this figure corresponds to a
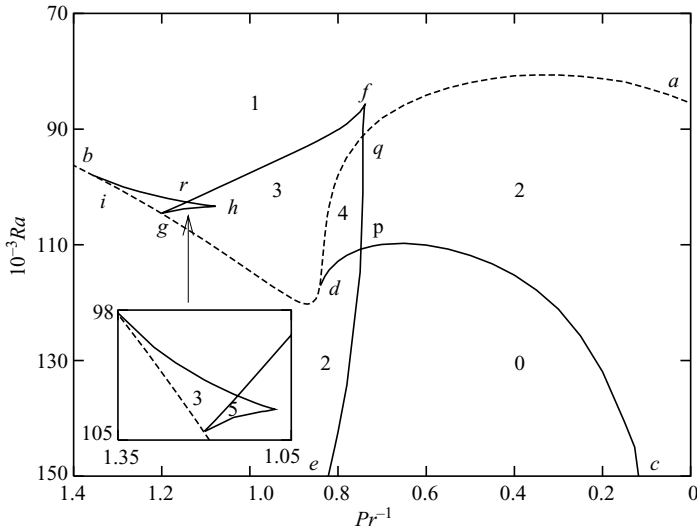
FIGURE 23. Parameter chart in the two-dimensional (Ra, Pr^{-1}) plane for the B_3 solution. The curves are bifurcation curves that separate regions in the plane where a different number of realizations of the B_3 flow pattern are possible. The numbers indicate the number of possible realizations of the B_3 flow pattern within each region. The dashed curve a–b identifies symmetry-breaking bifurcation points. The five solid curves c–d, e–f, f–g, g–h and h–i are fold curves. The intersection points of bifurcation curves are labelled p, q and r. The directions of the axis in this figure are reversed for consistency with figure 22.

curve of symmetry-breaking bifurcation points of the unstable flow pattern B_8. Hence, the B_3 solution manifold connects to the B_8 solution surface through this bifurcation curve. The other five curves in figure 23 are fold curves, i.e. curves formed by the loci of turning points. The cusp points labelled f, g and h in figure 23 correspond to codimension-two hysteresis points where two fold lines coalesce.

The bifurcation curves where the stability character of the B_3 solution changes are depicted as black solid lines over the solution surface in figure 22. This figure shows two different regions of stability, which correspond to the ranges $Pr^{-1} \leqslant 1.16$ ($Pr \geqslant 0.86$) and $Pr^{-1} \geqslant 1.24$ ($Pr \leqslant 0.81$), respectively. In the latter region the B_3 flow pattern becomes stable at considerably large values of Ra ($Ra \geqslant 90\,200$), but once it has become stable it remains so thereafter within the domain studied ($Ra \leqslant 1.5 \times 10^5$). On the contrary, within the region $Pr^{-1} \leqslant 1.16$ ($Pr \geqslant 0.86$) the B_3 flow pattern presents regions of stability at rather low values of Ra. The values of Ra at which the B_3 flow pattern becomes stable increase smoothly from $Ra = 20\,600$ to $Ra = 35\,000$ in this region. The nature of the bifurcation where B_3 becomes unstable depends on Pr in the region $Pr^{-1} \leqslant 1.16$ ($Pr \geqslant 0.86$). Specifically, B_3 becomes unstable as a consequence of a symmetry-breaking bifurcation that occurs at values of Ra within the range $79\,360 \leqslant Ra \leqslant 88\,050$ whenever Pr^{-1} is lower than 0.73 ($Pr > 1.37$). In the narrow region $0.73 \leqslant Pr^{-1} \leqslant 0.75$ ($1.33 \leqslant Pr \leqslant 1.37$) B_3 becomes unstable at the turning point over the fold line (f–e) in figure 23. Hence, the Rayleigh number at which B_3 becomes unstable increases rapidly from $Ra = 88\,050$ to $Ra = 114\,700$ within this region. Finally, in the region $0.75 \leqslant Pr^{-1} \leqslant 1.16$ ($0.86 \leqslant Pr \leqslant 1.33$) the value of Ra at which B_3 becomes unstable decreases smoothly from $Ra = 114\,700$ to $Ra = 35\,000$ and the instability is again due to a symmetry-breaking bifurcation.
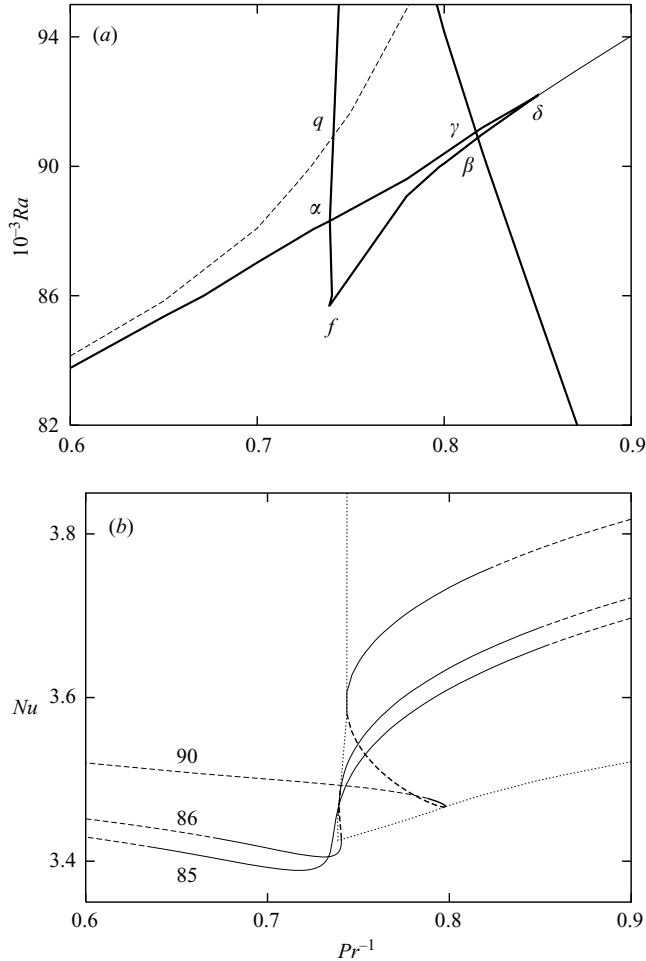
FIGURE 24. (a) Stability α–δ–f region for the B_3 flow pattern, which is not properly visualized in figure 22. The dashed line and the points labelled f and q correspond to the same line and points as in the parameter chart plotted in figure 23. Two realizations of the B_3 flow pattern are stable within the region α–γ–β–f. (b) Continuation curves over the B_3 solution surface at $Ra = 8.5 \times 10^4$, 8.6×10^4 and 9×10^4. The dotted curves correspond to the fold curves f–e and f–g in the parameter chart plotted in figure 23.

In addition, there is a third small region of stability which cannot be properly visualized in figure 22. This region is the quasi–triangular region α–δ–f in figure 24(a). Note that the point f corresponds to the cusp point depicted in figure 23. Two realizations of the B_3 flow pattern are simultaneously stable for values of Ra and Pr^{-1} within the region α–γ–β–f in figure 24(a). This issue is better illustrated in figure 24(b) where three tracked continuation solution curves are plotted. Note that the B_3 flow pattern is unstable within the whole Ra range investigated for $1.16 \leqslant Pr^{-1} \leqslant 1.24$ ($0.81 \leqslant Pr \leqslant 0.86$).

The development of the folds in the solution manifold near the cusp points g and h is shown in figure 25. The three curves plotted in this figure were obtained by a sequence of continuation runs using Pr^{-1} as the continuation parameter. It is clear that a saddle-like behaviour appears for Ra between 103×10^3 and 104×10^3.
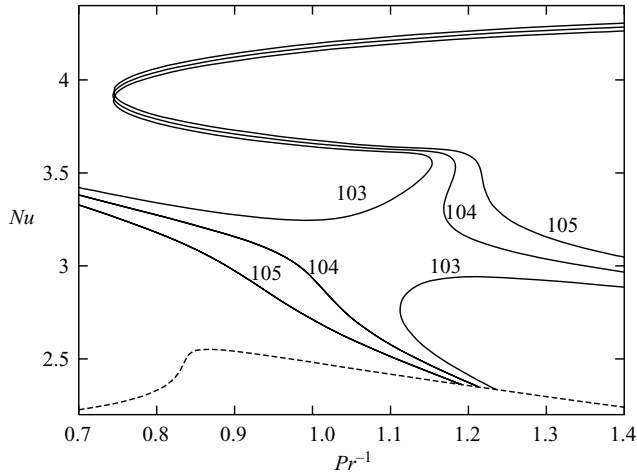
FIGURE 25. Development of the folds in the solution manifold near the cusp points g and h in figure 23. The curves plotted in this figure were obtained by a sequence of continuation runs using Pr^{-1} as a continuation parameter at $Ra = 103 \times 10^3$, 104×10^3 and 105×10^3. The dashed curve corresponds to the symmetry-breaking bifurcation curve in the parameter chart plotted in figure 23.

Figure 25 shows that five possible realizations of the B_3 flow pattern are possible for some values of Pr^{-1} at $Ra = 103 \times 10^3$ and $Ra = 104 \times 10^3$, in agreement with the parameter chart plotted in figure 23.

4. Conclusions

The bifurcation diagrams of steady flow patterns that develop inside a cubical cavity heated from below and filled either with air ($Pr = 0.71$) or silicone oil ($Pr = 130$) were determined by means of an arclength continuation procedure based on a Galerkin spectral method. The study was performed in the range $Ra \leqslant 1.5 \times 10^5$ and the four lateral walls were assumed to be perfectly conducting. Twenty-one and thirty-five solution branches were continued using Ra as parameter at $Pr = 0.71$ and $Pr = 130$, respectively. The stability analyses predicted that four (B_1, B_{11}, B_3, B_{312}) and nine steady flow patterns (B_1, B_2, B_{24}, B_{25}, B_{251}, B_{26}, B_3, B_{34}, B_5) were respectively stable at $Pr = 0.71$ and 130 over certain ranges of Ra in the region investigated. The spatial configurations of the flow patterns are very similar to those developed for adiabatic lateral walls at values of Ra close to the bifurcation point where they set in, but they become increasingly different as the Rayleigh number is increased. The greater complexity of the present problem, compared to the case with adiabatic lateral walls, is a direct consequence of the thermal activity of the lateral walls.

Comparison of the bifurcation diagrams at $Pr = 0.71$ and 130 shows that the evolution of flow patterns and their stability are strongly dependent on the Prandtl number. Flow patterns tend to adopt a double toroidal spatial configuration, even at moderate values of Ra when the cavity is filled with silicone oil ($Pr = 130$). This double toroidal configuration consists of two torus-like vortices that respectively span most of the top and bottom halves of the cavity. The thermal activity of the sidewalls is the reason why almost every flow pattern, especially at $Pr = 130$, tends to adopt the double toroidal topology as the Rayleigh number increases.

The variation of the heat transfer rate at the bottom plate as a function of the two control parameters Ra and Pr^{-1} for the flow pattern B_3 with an initial four-connected-half-roll configuration yielded a rather complex three-dimensional manifold that presented several folds and cusp points. The presence of folds in the solution manifold reveals that up to five realizations of the B_3 flow pattern are possible over some ranges of the parameters Ra and Pr^{-1} and that even two stable realizations coexist over a narrow region of these parameters. This explains the important differences in the spatial configuration and in the stability character of the B_3 flow pattern at different Prandtl numbers.

The present calculations are in fairly good agreement with the experimental results reported by Leong *et al.* (1999) at $Pr = 0.71$ and Pallarès *et al.* (2001) at $Pr = 130$. The current analysis provides a possible interpretation for the two different values of the heat transfer at the bottom plate, Nu_h, reported by Leong *et al.* (1999) at $Ra = 10^5$. In addition, it explains most of the experimental flow transitions between different steady flow patterns observed by Pallarès *et al.* (2001) over the region $Ra \leqslant 8 \times 10^4$ at $Pr = 130$.

REFERENCES

AHLERS, G. 2000 Effect of sidewall conductance on heat–transport measurements for turbulent Rayleigh–Bénard convection. *Phys. Rev.* E **63**, 015303.

BERGEON, A., HENRY, D. & KNOBLOCH, E. 2001 Three-dimensional Marangoni-Bénard flows in square and nearly square containers. *Phys. Fluids* **13**, 92–98.

BODENSCHATZ, E., PESCH, W. & AHLERS, G. 2000 Recent developments in Rayleigh-Bénard convection. *Annu. Rev. Fluid Mech.* **32**, 709–778.

CATTON, I. 1970 Convection in a closed rectangular region: the onset of motion. *Trans. ASME: J. Heat Transfer* **92**, 186–188.

CATTON, I. 1972 The effect of insulating vertical walls on the onset of motion in a fluid heated from below. *Intl J. Heat Mass Transfer* **15**, 665–672.

CRAWFORD, J. D. & KNOBLOCH, E. 1988 On degenerate Hopf bifurcation with broken O(2) symmetry. *Nonlinearity* **1**, 617–652.

CRAWFORD, J. D. & KNOBLOCH, E. 1991 Symmetry and symmetry-breaking bifurcations in fluid dynamics. *Annu. Rev. Fluid Mech.* **23**, 341–387.

DAVIS, S. H. 1967 Convection in a box: linear theory. *J. Fluid Mech.* **30**, 465–478.

GELFGAT, A. Y. 1999 Different modes of Rayleigh–Bénard instability in two and three dimensional rectangular enclosures. *J. Comput. Physics* **156**, 300–324.

GETLING, A. V. 1998 *Rayleigh-Bénard Convection: Structures and Dynamics*. World Scientific.

GOLUBITSKY, M., STEWART, I. & SCHAEFFER, D. G. 1988 *Singularities and Groups in Bifurcation Theory*. Springer.

HARRIS, D. L. & REID, W. H. 1958 On orthogonal functions which satisfy four boundary conditions. *Astrophys. J. Supp.* **3**, 429–452.

JEONG, J. & HUSSAIN, F. 1995 On the identification of a vortex. *J. Fluid Mech.* **285**, 69–94.

KESSLER, R. 1987 Nonlinear transition in three–dimensional convection. *J. Fluid Mech.* **174**, 357–379.

KOSCHMIEDER, E. L. 1993 *Bénard Cells and Taylor Vortices*. Cambridge University Press.

LEHOUCQ, R. B. & SORENSEN, D. C. 1996 Deflation techniques for an implicitly restarted Arnoldi iterations. *SIAM J. Matrix Anal. Appl.* **17**, 789–821.

LEONG, W. H., HOLLANDS, K. G. T. & BRUNGER, A. P. 1998 On a physically–realizable benchmark problem in internal natural convection. *Intl J. Heat Mass Transfer* **41**, 3817–3828.

LEONG, W. H., HOLLANDS, K. G. T. & BRUNGER, A. P. 1999 Experimental Nusselt numbers for a cubical-cavity benchmark problem in natural convection. *Intl J. Heat Mass Transfer* **42**, 1979–1989.

MIZUSHIMA, J. & MATSUDA, O. 1997 Onset of 3D thermal convection in a cubic cavity. *J. Phys. Soc. Japan* **66**, 2237–2341.

MIZUSHIMA, J. & NAKAMURA, T. 2003 Onset of three–dimensional thermal convection in a rectangular parallelepiped cavity. *J. Phys. Soc. Japan* **72**, 197–200.

MORGAN, R. B. 1996 On restarting the Arnoldi method for large nonsymmetric eigenvalue problems. *Maths. Comput.* **65**, 1213–1230.

PALLARÈS, J., ARROYO, M. P., GRAU, F. X. & GIRALT, F. 2001 Experimental laminar Rayleigh-Bénard convection in a cubical cavity at moderate Rayleigh and Prandtl numbers. *Exps. Fluids* **31**, 208–218.

PEPPER, D. W. & HOLLANDS, K. G. T. 2002 Summary of benchmark numerical studies for 3D natural convection in an air–filled enclosure. *Numerical Heat Transfer* A **42**, 1–11.

PUIGJANER, D. 2005 Study of a natural convection problem inside a cubical cavity from the point of view of dynamical systems. PhD thesis, Facultat de Matemàtiques, Universitat de Barcelona, Barcelona. Spain.

PUIGJANER, D., HERRERO, J., GIRALT, FRANCESC & SIMÓ, C. 2004 Stability analysis of the flow in a cubical cavity heated from below. *Phys. Fluids* **16**, 3639–3655.

PUIGJANER, D., HERRERO, J., GIRALT, FRANCESC & SIMÓ, C. 2006 Bifurcation analysis of multiple steady flow patterns for Rayleigh–Bénard convection in a cubical cavity at $Pr = 130$. *Phys. Rev. E* **73**, 046304.

ROCHE, P. E., CASTAING, B., CHABAUD, B., HÉBRAL, B. & SOMMERIA, J. 2001 Side wall effects in Rayleigh-Bénard experiments. *Eur. Phys. J.* B **24**, 405–408.

SÁNCHEZ, J., NET, M., GARCÍA-ARCHILLA, M. B. & SIMÓ, C. 2004 Newton-Krylov continuation of periodic orbits for Navier-Stokes flows. *J. Comput. Physics* **201**, 13–33.

SIMÓ, C. 1990 Analytical and numerical computation of invariant manifolds. In *Modern methods in Celestial Mechanics* (ed. D. Benest & C. Froeschlé), pp. 285–330. Editions Frontières.

VERZICCO, R. 2002 Sidewall finite–conductivity effects in confined turbulent thermal convection. *J. Fluid Mech.* **473**, 201–203.

YANG, K. T. 1988 Transitions and bifurcations in laminar buoyant flows in confined enclosures. *Trans. ASME: J. Heat Transfer* **110**, 1191–1204.